

UNCLASSIFIED

AD NUMBER
AD865522
NEW LIMITATION CHANGE
TO Approved for public release, distribution unlimited
FROM Distribution authorized to U.S. Gov't. agencies only; Critical Technology; AUG 1969. Other requests shall be referred to Air Force Cambridge Research Laboratories, L.G. Hanscom Field, Bedford, MA 01730.
AUTHORITY
AFCRL ltr, 22 Dec 1971

THIS PAGE IS UNCLASSIFIED

AD 865522

AFCRL-69-0354
AUGUST 1969
PHYSICAL SCIENCES RESEARCH PAPERS, NO. 394



MICROWAVE PHYSICS LABORATORY PROJECT 4642

AIR FORCE CAMBRIDGE RESEARCH LABORATORIES

L. G. HANSCOM FIELD, BEDFORD, MASSACHUSETTS

This document is approved
for public release and its
distribution is unlimited.

Effects of the Reentry Plasma Sheath on Microwave Antenna Performance: Trailblazer II Rocket Results of 18 June 1967

J. LEON POIRIER
WALTER ROTMAN
DALLAS T. HAYES
JOHN F. LENNON

This document is subject to special export
control and each distribution should be
monitored for foreign release. No release
prior approval of AFCRL, ERD, L.G. Hanscomb
Field, Bedford, Massachusetts.

OFFICE OF AEROSPACE RESEARCH
United States Air Force



Abstract

An AFCRL Trailblazer II rocket was launched on 18 June 1967 from the NASA Wallops Island (Va.) Rocket Test Facility to study the properties of the reentry plasma sheath and its effects on microwave antenna performance. The reentry payload consisted of three major subsystems: a plasma diagnostic system, an S-band transponder system, and an X-band telemetry system. The flight data yielded (1) measurements of the influence of the plasma on the radiation pattern distortion, signal attenuation, and impedance mismatch for an S-band slot antenna located at the stagnation point of the nose cone; (2) measurements of the plasma sheath effects on the interantenna coupling between two S-band antennas on the nose cone; and (3) determinations of the electron density profile and gradients in the boundary layer about the nose cone.

These measurements indicated that electron density profiles in the flow fields can be determined from electrostatic and electroacoustic probe data. The microwave antenna data was in substantial agreement with the probe data and flow field calculations, with the best agreement obtained at altitudes below 240 kft. The shape of the radiation patterns of the S-band antennas remained invariant with altitude, in accord with the theory of microwave interaction with a thin plasma layer.

Contents

1. INTRODUCTION	1
1.1 The Reentry Communications Problem	2
1.2 Flight Test Objectives	3
2. INSTRUMENTATION AND PAYLOAD	3
2.1 Vehicle and Nose Cone	3
2.2 Payload Description	4
2.3 Payload Subsystems	11
2.3.1 Electroacoustic Probes	11
2.3.2 Electrostatic Probes	12
2.3.3 Telemetry	13
3. TRAJECTORY AND FLOW FIELD ANALYSES	13
3.1 Flight History	14
3.2 Spin and Precession	15
3.3 Angle of Attack	17
3.4 Antenna Polar Angle	18
3.5 Flow Field Calculations	19
4. PROBE THEORY AND RESULTS	22
4.1 Electrostatic Probe Theory	23
4.2 Electroacoustic Probe Theory	26
4.3 Electrostatic Probe Results	30
4.4 Electroacoustic Probe Results	35
4.5 Comparison of EA and ES Results	38
5. S-BAND SLOT ANTENNA STUDIES	39
5.1 Antenna Admittance and Coupling	39
5.2 Signal Attenuation and Radiation Patterns	48

Contents

6. DISCUSSION	52
7. CONCLUSIONS	53
ACKNOWLEDGMENTS	55
REFERENCES	57
APPENDIX A: Plasma Sheath Data for Slot Antenna Calculations	A1
APPENDIX B: Polarization Factor for Radiation Pattern of Nose Cone Antenna	B1

Illustrations

1. Trailblazer II Profile	5
2. Typical Staging History	5
3. Photograph of Instrumented Nose Cone	5
4. Sketches Showing Antenna and Probe Locations on Nose Cone	6
5. Simplified Block Diagram of S-band Experiment	7
6. Cross-section Drawing of S-band Antennas	7
7. Breakdown Data for Nose Cap Transmitting Antenna	9
8. Three Views of Instrumentation Package	10
9. Block Diagram of Electroacoustic Probe Electronics	11
10. Cross-section Drawing of Electroacoustic Probe	12
11. Cross-section Drawing of Electrostatic Probe	13
12. Actual and Predicted Planar Trajectories	14
13. Reentry History	15
14. Electrostatic Probe Measurement of Spin and Precession	17
15. North-South Velocity Component Before and After Fourth-Stage Firing	18
16. Electron Density Profiles in the Stagnation Region	21
17. Stagnation Streamline Electron Density and Collision Frequency Distributions Around the Body	22
18. Electron Density Profile in Plasma Sheath	27
19. Intensity of Electroacoustic Resonances Versus Gas Pressure	29
20. Voltage Measured by Electrostatic Probe No. 3 Versus Altitude	31
21. Electron Density at Edge of Boundary Layer Versus Altitude [<u>(a)</u> electrostatic probe No. 2, <u>(b)</u> electrostatic probe No. 3]	33

Illustrations

22.	Electron Density at Separation of r_s From Vehicle Surface Versus Altitude [(a) electrostatic probe No. 2, (b) electrostatic probe No. 3]	33
23.	Reflected Power Versus Altitude for 400-MHz Electroacoustic Probe ($S/R_n = 2.72$)	35
24.	Electron Density Profile Measured by (a) the 1500-MHz Electroacoustic Probe, (b) the 400-MHz Electroacoustic Probe	38
25.	Dimensions of Nose Cone Slot Antenna	39
26.	Self and Input Admittances of Nose Cone Slot Antenna	41
27.	Equivalent Circuit for Slot Antenna	42
28.	Power Reflection Coefficient Versus Altitude for Nose Cone Slot Antenna	43
29.	Electromagnetic Boundary Layer Thickness δ Versus Altitude	45
30.	Power Reflection Coefficient Versus Boundary Layer Thickness for Slot Antenna	45
31.	Mutual Coupling Loss Versus Altitude for Two Slot Antennas on Nose Cone	45
32.	Network Diagram for Conjugate Admittance Theorem	46
33.	Coordinate System for Radiation Patterns of Slot Antenna	49
34.	Theoretical Radiation Pattern of Slot in Ground Plane	50
35.	Freospace Radiation Patterns for Trailblazer II Nose Cone Antenna	50
36.	Received Signal Intensity Versus Altitude for Slot Antenna on Nose Cone	50
37.	Radiation Patterns Versus Altitude: Trailblazer II Flight Data	52
B1.	Polarization Diagrams for Radiation Patterns	B2

Tables

1.	Plasma Parameters for Electroacoustic Resonance	37
A1.	Electrical Properties of Plasma Layers at Stagnation Point of Nose Cone	A2
A2.	Admittance and Isolation of Slot Antennas Versus Altitude	A3
A3.	Parametric Variation in Electrical Properties of Plasma Layers at Stagnation Point (altitude = 240 kft)	A4
A4.	Parametric Variation in Admittance and Reflection Coefficient of Slot Antennas (altitude = 240 kft)	A5

Effects of the Reentry Plasma Sheath on Microwave Antenna Performance: Trailblazer II Rocket Results of 18 June 1967

1. INTRODUCTION

Any aerospace vehicle that traverses the upper atmosphere at very high velocities becomes enveloped by a shock-ionized flow field—a plasma sheath—that can severely degrade the quality of radio signals transmitted or received by the vehicle during the critical terminal part of the flight. To find techniques for improving radio transmission from aerospace reentry and other high-altitude vehicles, AFCRL has instituted a research program designed to explore this multifaceted problem by means of theoretical analyses, laboratory experiments, and rocket flight tests.

The flight tests depend on scientific payloads carried aboard Trailblazer II vehicles to measure plasma and antenna characteristics, antenna voltage breakdown, and several other parameters relevant to transmission through the plasma sheath during reentry. The interaction of microwave radiation with shock-ionized flow fields is assessed from the data thus obtained. The effect of the plasma sheath on microwave antenna performance is then evaluated; and the properties of a plasma that influence its response to incident microwave radiation are determined.

(Received for publication 18 August 1969)

The studies include in-flight measurements of the radiation patterns and impedance of plasma-covered antennas, aimed at defining the conditions of high-input power under which the antenna can break down.

1.1 The Reentry Communications Problem

Studies conducted at AFCRL and elsewhere (Aerospace Corporation, 1966; Rotman et al, 1967, 1964; Balyanski, 1967; Proceedings, 1967) have shown that radiowaves can penetrate the plasma sheath around reentry vehicles at either (1) very high frequencies when the operating frequency exceeds that of the plasma, or (2) very low frequencies when the skin depth (a function of wavelength) is much greater than that of the plasma sheath. For future aerospace systems required by lifting reentry vehicles, these frequencies correspond to those below 1 MHz or above 10 CHz. The low-frequency regime has limited value because the information capacity of these transmission links is restricted by the very narrow bandwidth of the electrically small aerospace antennas; the high-frequency approach is limited because of radiowave attenuation caused by atmospheric absorption and because of the restricted range of present-day millimeter-wave systems. In general, operation at the highest practical frequency enhances penetration of the plasma sheath, and application of other techniques such as the use of chemical additives is simplified since these aerospace antennas are smaller in size.

A reentry vehicle masked by a plasma whose frequency falls into the millimeter-wavelength range presents a difficult problem in communications. At these wavelengths, water vapor absorption is particularly severe. An all-weather aerospace-ground communications link is therefore ineffective; but since practically all atmospheric absorption is encountered at altitudes below 20000 ft, a millimeter-wave link between a reentry vehicle and an airborne communications station is feasible (Baldwin et al, 1961). For clear-weather operation, it is possible to make use of the radiofrequency 'window' that is present in the atmosphere at about 35 GHz.

The use of optical wavelengths—of current interest since invention of the laser—is likewise restricted to either clear-weather operation or airborne receiving sites. Other techniques that offer some promise of improving reentry communications, such as modifying the plasma with chemical additives, are under active investigation.

Reentry communication studies have been limited by lack of suitable environmental facilities for simulating reentry conditions. Shock tunnels have very short test periods, and wind tunnels cannot simultaneously achieve the required flow velocity and enthalpy. Ballistic ranges can fire only relatively small reentry

models that are difficult to instrument and for which scaling parameters are not readily available. Static or seeded plasmas have proved to be valuable tools but do not simulate all parameters. Although considerable progress in reentry simulation facilities has been made during the last five years, all the important factors affecting reentry communications cannot be reproduced within laboratory facilities. For this reason, flight-test programs are necessary to validate ground-based experiments and theoretical analysis of plasma sheath effects, and to evaluate specific alleviation techniques.

1.2 Flight Test Objectives

For the first AFCRL Trailblazer II payload, launched from NASA's Wallops Island (Va.) Rocket Test Facility on 18 June 1967, the following four objectives were established:

- 1) Measure the influence of the plasma sheath on radiation pattern distortion, signal attenuation, and impedance mismatch (S-band slot antenna located at the stagnation point of the nose cone).
- 2) Measure plasma sheath effects on interantenna coupling (two S-band antennas on the nose cone).
- 3) Determine the electron density profile and gradients about the nose cone by means of electrostatic and electroacoustic probes respectively.
- 4) Measure the effects of high-power microwaves on: (a) plasma sheath properties, (b) antenna voltage breakdown, (c) nonlinear pulse shape distortion.

The first three test objectives were achieved. The analyses of the test data are presented in this report, following a discussion of the reentry payload design.

2. INSTRUMENTATION AND PAYLOAD

2.1 Vehicle and Nose Cone

The Trailblazer II vehicle (Figure 1) is a four-stage solid-propellant rocket that achieves high reentry velocities. After the first two stages drive the vehicle to an altitude of about 200 miles, the last two propel the reentry nose back toward the atmosphere in an almost vertical trajectory.

During the ascending part of the flight the vehicle is fin-stabilized. Shortly after launch, the canted second-stage fins induce spinning, and as the vehicle leaves the atmosphere its spin rate is high enough to ensure that it will be spin-stabilized at an angle of 68° throughout the remainder of the flight.

The last two stages are enclosed in a structural shell (velocity package) and face forward during launch. At about 250 kft, the velocity package separates

from the spent second-stage motor and coasts to apogee. As the velocity package begins its descent the X-248 third-stage motor fires, propelling the reentry nose cone out of the open end of the velocity package. The 15-in. fourth-stage spherical motor provides the final thrust necessary to boost the nose cone velocity to about 17,000 fps. A typical staging history of a flight is shown in Figure 2.

The reentry nose cone shown in Figure 3 is a 9° hemisphere-cone fabricated entirely of aluminum. Its dimensions are: nose cap radius, 6.333 in.; total length, 26.47 in.; base diameter, 19.17 in. The instrumented nose weighs about 65 lb, including the spent fourth-stage motor, which remains within the reentry body. So that the measured plasma characteristics can be compared with the values predicted from flow-field calculations, the heat-sink method of thermal protection (no ablative coatings) is used to ensure that the flow about the vehicle is not contaminated with ablation products.

2.2 Payload Description

The payload was instrumented to make S-band frequency measurements of nonlinear distortion of pulse shape, interantenna coupling (including nonlinear effects), antenna impedance mismatch, voltage breakdown, radiation pattern distortion, and plasma sheath attenuation. Electron density was measured with flushmounted electrostatic probes and gradients were measured with electroacoustic probes. The diagnostic probes were made an integral part of the microwave radiation experiment so that the exact properties of the plasma and their effects on the antenna system could be simultaneously determined. An X-band pulse-position-modulation (PPM) telemetry system relayed the in-flight data to the ground receiving stations. The sketches in Figures 4 show (a) the nose cone and (b) the location of the antennas and probes.

The simplified block diagram in Figure 5 describes the S-band experiment. The transponder has a superheterodyne receiver connected to the shoulder antennas S2 and S3 and a 1.5-kW transmitter operating through the nose cap antenna S1. Instead of one common antenna, separate receiving and transmitting antennas (Figures 6) are used to ensure that the incoming radar interrogation signal is not severely attenuated by the plasma sheath. The plasma density at the shoulder antennas (S2 and S3) is considerably less than at the stagnation point. The receiver therefore continues to be interrogated even after the nose cap antenna has been completely blacked out, and such on-board measurements of the nose cap antenna as mismatch, coupling, and breakdown, can continue to be made even after blackout.

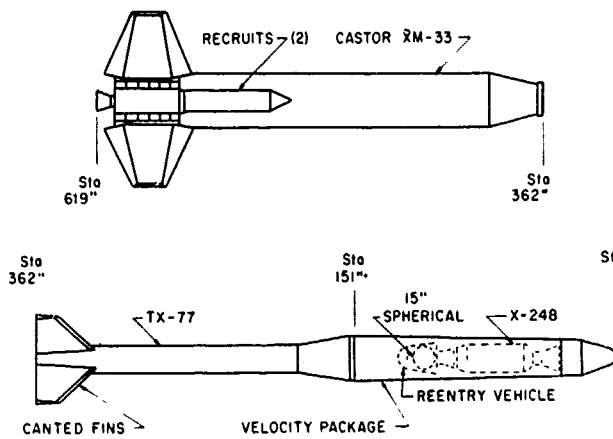


Figure 1. Trailblazer II Profile

Figure 2. Typical Staging History

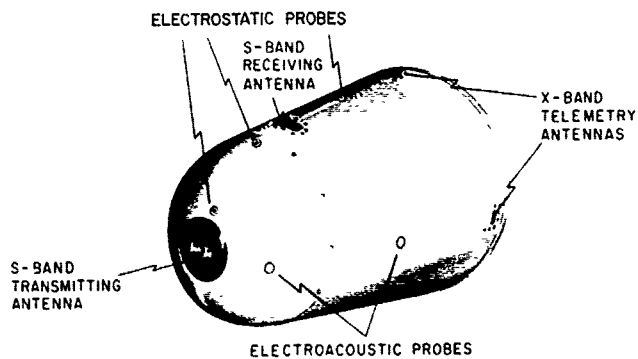
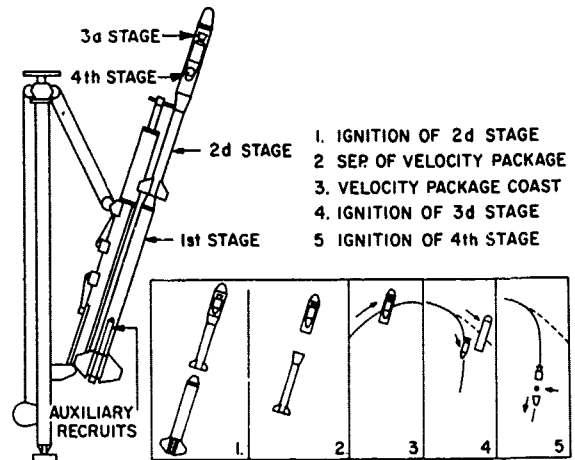
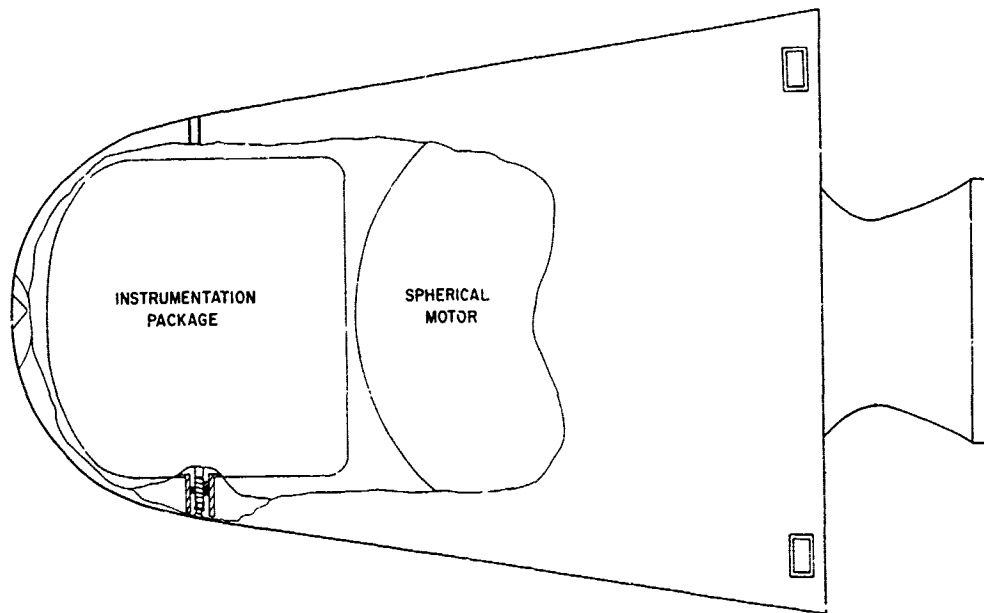
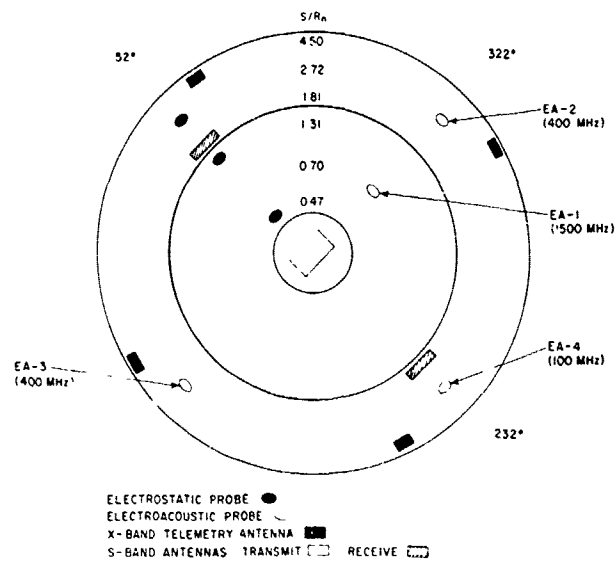


Figure 3. Photograph of Instrumented Nose Cone



(a)



(b)

Figure 4. Sketches Showing Antenna and Probe Locations on Nose Cone [(a) side view, (b) end view. The ratios listed under S/R_n give the peripheral distance S from the central axis to the location of the sensor normalized with respect to the nose cap radius R_n .]

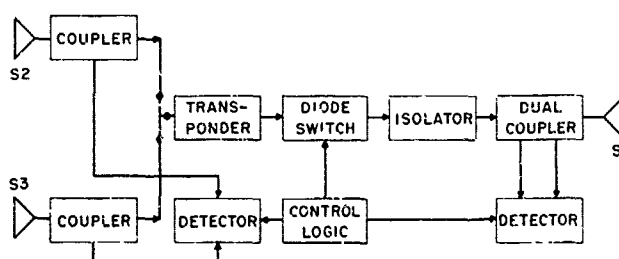


Figure 5. Simplified Block Diagram of S-band Experiment

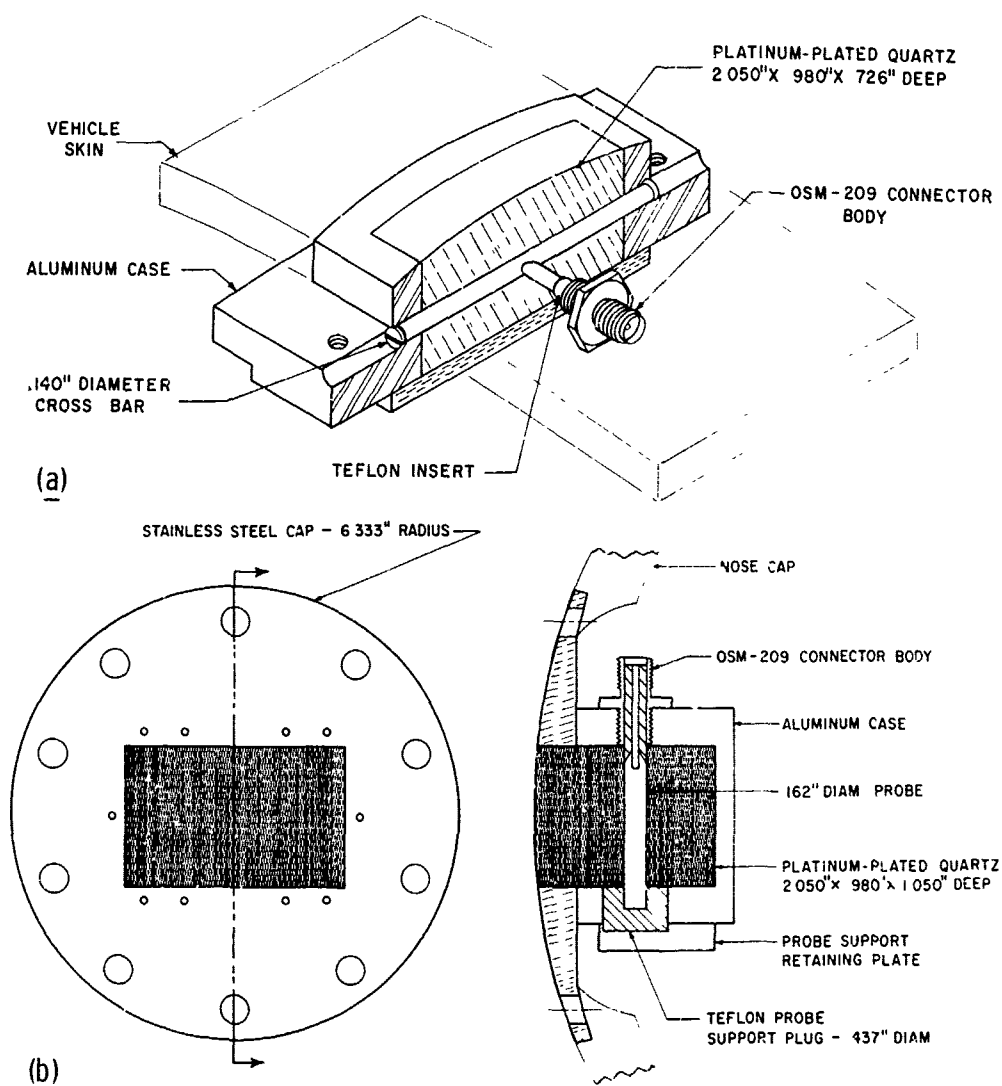


Figure 6. Cross-Section Drawing of S-band Antennas
[(a) receiving antenna, (b) transmitting antenna]

Nonlinear characteristics of the plasma are determined by comparing measurements taken at several different power levels. To accomplish this the transmitter is connected to its antenna through a diode step attenuator and a dual directional coupler. The function of the diode switch is to attenuate the transmitter signal such that the antenna input power is sequentially switched from 1 kW to 500 W and then to 125 W; the dual directional coupler is used for monitoring operation of the nose cap antenna. Both coupler outputs are detected in peak and average detectors.

The directional couplers in the transmission lines of the receiving antennas are used for sampling the power coupled to these antennas from the nose cap antenna. These couplers also work into both peak and average detectors.

Attenuator switching and detector sampling are controlled by the logic module, which uses the 20-pps frame-synchronization signal of the commutator as a clock. The attenuator switching signal is half the clock frequency, and the transponder is interrogated by the ground radar at the rate of 320 pps. A set of transmitted pulses consists of three 32-pulse groups, one at each of the three selected power levels.

The attenuator switching signal also resets a counter in the logic module. This counter keeps track of the transmitted pulses and gates the detectors on at the proper point within each group of pulses. Just before the end of the group, the gates are closed, the detector outputs are sampled, and the detector holding circuits are discharged. The process is repeated for each power level.

The repetition and switching rates were chosen to ensure at least one complete revolution of the nose cone during a group period and that the altitude change during a set of three groups would be small enough to prevent any significant change in plasma characteristics. This was done so that both high-power and low-power values could be measured simultaneously.

The S-band antennas (Figures 6) are quartz-filled cavity-backed slot antennas. The transmitting antenna is probe-fed and the receiving antennas are of the cross-bar type. As a precaution against detuning due to unequal expansion of the quartz and cavity walls during flight and to ease the tolerances at final assembly, the quartz dielectric blocks have a 0.005-in.-thick platinum coating on all faces except the aperture face. The effective electrical cavity walls are thus formed by platinum surfaces in intimate contact with quartz.

Breakdown characteristics of the nose-cap antenna were determined by a series of bell-jar measurements. The measured curve (Figure 7) indicates that breakdown occurs at 140 kft with a minimum antenna input power of about 800 W. The presence of plasma significantly reduces the minimum power required for breakdown during reentry.

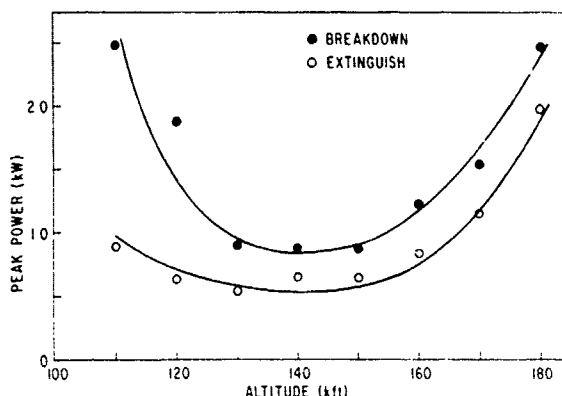


Figure 7. Breakdown Data for Nose Cap Transmitting Antenna

Complete radiation patterns, in the form of contour plots, were made of all antennas prior to the flight for later comparison with the in-flight antenna patterns. Photographs of the major components of the S-band system are shown in Figures 8. The detector is a crystal followed by a single-stage FET amplifier.

On the ground, the transponder reply pulses are displayed together with the range timing signals on a calibrated oscilloscope that is synchronized by the radar range gate. Photographing this display on a pulse-by-pulse basis yields a record that makes it possible to instantaneously correlate the S-band pulses received on the ground with the onboard data relayed to the ground over the X-band telemetry link.

By comparing the photographic records of the behavior of the system at the three power levels, it is possible to determine antenna voltage breakdown (evidenced by a severe distortion of the pulse shape), plasma sheath attenuation, and antenna pattern distortion and other nonlinear effects. The nose cone measurements relayed to the ground over the telemetry link are used to determine antenna impedance mismatch and interantenna coupling. A comparison of the outputs of the peak and average detectors of the directional coupler monitoring the reflected power of the transmitting antenna identifies antenna voltage breakdown: under breakdown conditions there is almost no change in the output of the peak detector but there is a significant decrease in the output of the average detector.

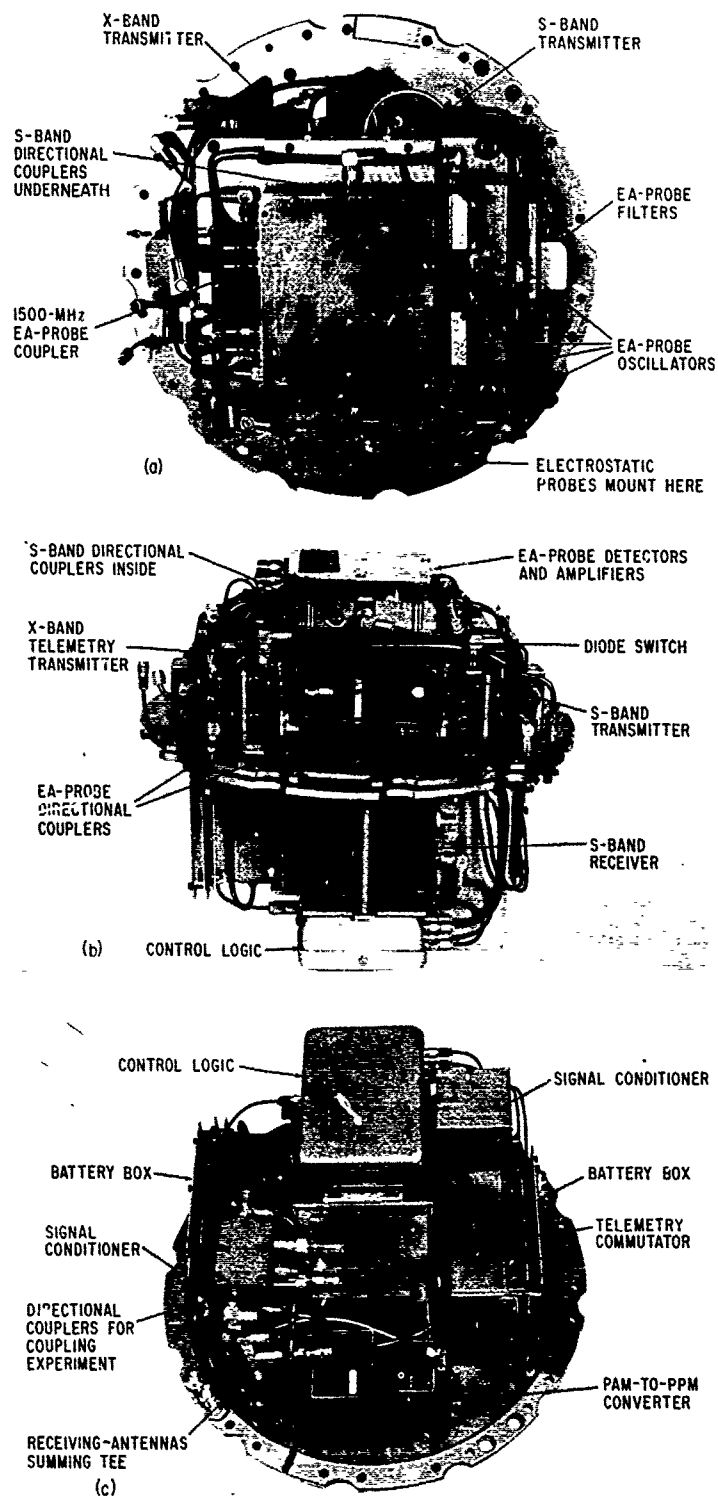


Figure 8. Three Views of Instrumentation Package [(a) top, (b) side, (c) bottom]

2.3 Payload Subsystems

2.3.1 ELECTROACOUSTIC PROBES

A new diagnostic tool, the electroacoustic (EA) probe, was flown for the first time in this experiment. The operating frequencies and locations of the four EA probes used were chosen to obtain measurements of the electron density gradient over a range of altitudes.

Probe EA1 (1.5 GHz) is mounted on the nose cap, probes EA2 and EA3 (400 MHz) are located on opposite sides of the nose cone at body location $S/R_n = 2.72$, EA4 (100 MHz) is mounted midway between probes EA2 and EA3 [Figure 4(b)]. The two identical probes mounted opposite each other on the nose cone allow detection of electron density variations arising from a nonzero angle of attack.

As indicated in Figure 9, each EA probe system consists of a low-power cw oscillator, typically 20 mW, connected to a flushmounted coaxial probe through a 20-dB directional coupler. The low-pass filter isolates the crystal detector from the S-band and X-band signals externally coupled into the probe from the payload transmitters.

The probes are designed to produce strong fringing fields that excite radio-frequency electroacoustic waves that travel at the speed of sound. In the absence of plasma, almost all of the power incident on the probe is reflected back to the detector. But when the probe surface and the plasma region whose frequency is equal to the operating frequency are separated by a distance that satisfies a resonance condition, the power reflected from the probe decreases sharply. By studying the power reflected from the probe it is possible to accurately determine

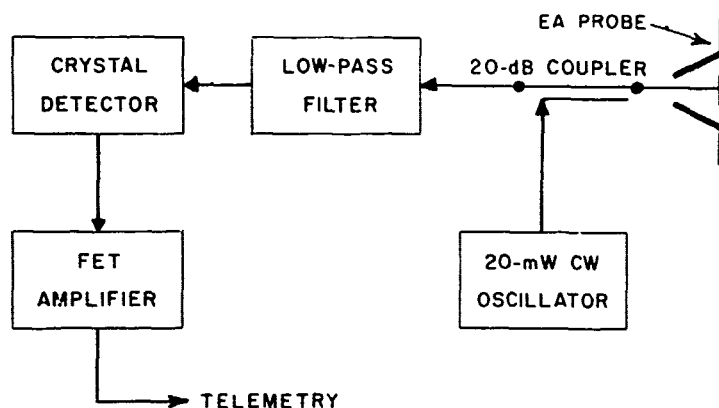


Figure 9. Block Diagram of Electroacoustic Probe Electronics

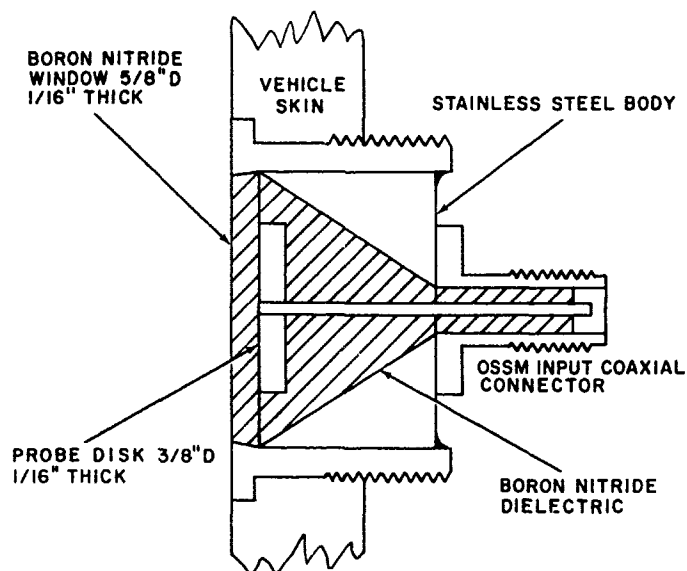


Figure 10. Cross-section Drawing of Electroacoustic Probe

the electron density gradient of the plasma sheath immediately adjacent to the sensing probe. For each probe the conditions required for resonance recur several times during a flight.

The flushmounted probe sketched in Figure 10 shows a basically coaxial device in which the tapered outer conductor is made of stainless steel. The internal and external insulators are both made of hot-pressed boron nitride. The probe connector is a subminiature 50-ohm OSSM panel jack, used with an 0.085-in.-diameter semirigid coaxial cable. The design is not critical so long as the resulting structure has strong fringing fields. The probe shown in Figure 10 was used at both 1.5 GHz and 400 MHz, but for 100 MHz, the diameter of the probe was doubled in order to increase its coupling to the plasma.

2.3.2 ELECTROSTATIC PROBES

To obtain additional information on the plasma density over the vehicle surface, three electrostatic probes were flushmounted on the reentry nose cone. Each probe consisted of a 0.25-in.-diam. iridium-plated molybdenum electrode insulated from the vehicle skin by a boron nitride dielectric (Figure 11). These probes are negatively biased (-15V) positive-ion probes that work into logarithmic amplifiers to yield good sensitivity over a wide dynamic range.

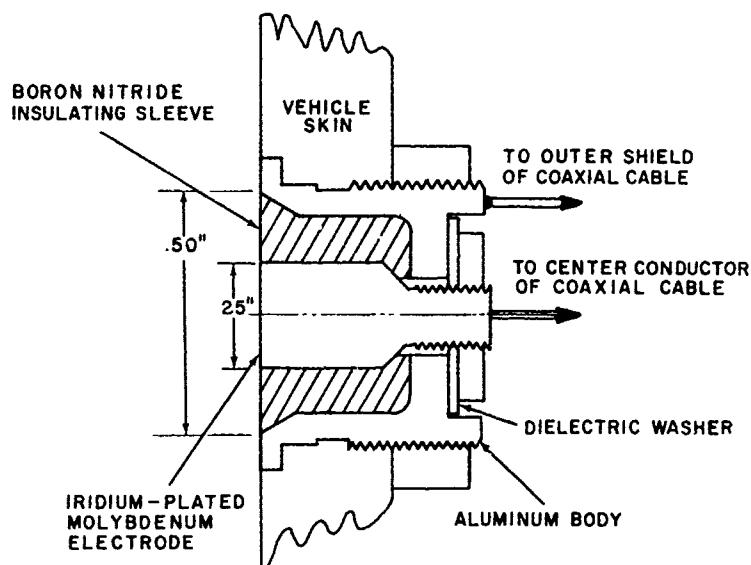


Figure 11. Cross-section Drawing of Electrostatic Probe

2.3.3 TELEMETRY

The X-band telemetry was a PPM system operated at 9210 MHz. The transmitter was connected to four quartz-covered waveguide antennas located near the rear edge of the nose cone (Figure 4) and triggered by a PAM-to-PPM converter driven by a standard 45-channel commutator. At a power level of 200W it produced 0.8- μ sec pulses. In the photographs of the telemetry system components shown in Figures 8, the payload has been assembled and wired except for the dc power connections.

3. TRAJECTORY AND FLOW FIELD ANALYSES

The following sections deal with the flight dynamics and plasma characteristics observed during the Trailblazer II flight of 18 June 1967. The performance, trajectory, and orientation of the vehicle are discussed in Secs. 3.1 to 3.4. The flow fields and the various properties of the ionized sheath surrounding the nose cone of the vehicle are discussed in Sec. 3.5. This material provides the background information for analysis of the various experiments functioning during the reentry flight.

3.1 Flight History

Two important respects in which the rocket performance differed from pre-launch predictions were: apogee was 100 kft lower, and burnout of the downward-oriented third-stage motor occurred 9 sec earlier. The change in trajectory and the shorter firing time resulted in a final reentry velocity of only 13,500 fps instead of the predicted 17,500 fps. Because of the lower velocity, aerodynamic heating was reduced, electron densities in the plasma sheath were lower, and the vehicle payload was still functioning below 125 kft, the altitude at which destruction had been anticipated.

Information on the vehicle trajectory came from various radar tracking records. The Spandar S-band and the AN/FPS-16 C-band radars relayed some information, but most of the significant period of the flight was covered by the AN/FPQ-6 C-band radar. At Wallops Island the radar returns were smoothed and processed, with the effects of the earth's curvature included in the computations. The output showed altitude, slant range, horizontal range, velocity components, and azimuthal position, but some parameters were not specified for every interval because there were gaps in the data.

Figure 12 compares the predicted trajectory with the overall trajectory based on the radar returns. The payload reentry was considered to have begun at 300 kft, which corresponded to 392.75 sec after launch. The variation in

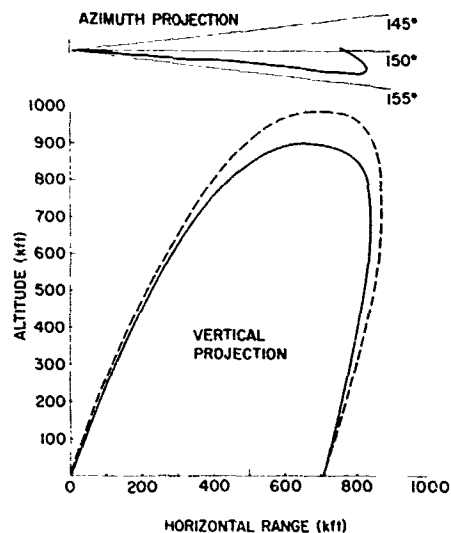


Figure 12. Actual and Predicted Planar Trajectories
(—— actual; ---- predicted)

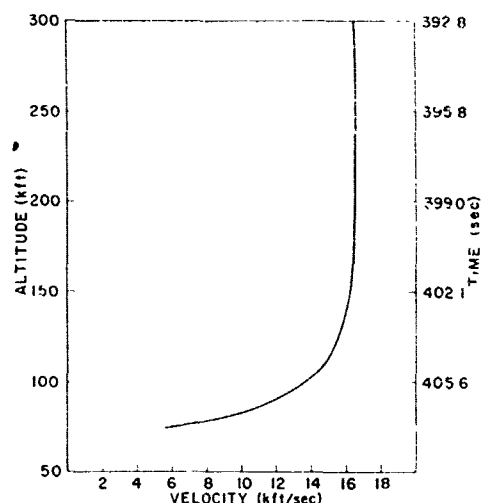


Figure 13. Reentry History

velocity during reentry, plotted versus altitude and versus time, is shown in Figure 13. The peak reentry velocity, 16,595 fps, was reached at an altitude of 220 kft.

The AN/FPQ-6 radar tracked the payload down to around 70 kft. Here the radar values became erratic, and it is assumed that at least partial deterioration of the vehicle occurred at this point.

3.2 Spin and Precession

Further analysis of the radar and telemetry data elicited information about the spin of the vehicle and the orientation of the vehicle with respect to the flight path. The rate of spin of the Trailblazer was determined from the rate of change in the radiation pattern of the S-band transmitting antenna in the vehicle nose. Since the radiated fields were linearly polarized, the spin caused the signal received at the ground station to oscillate from a maximum (when the polarization vectors were aligned) to a minimum one-quarter revolution later (when the polarization vectors were orthogonal). The periodicity of the signal shortly after the fourth-stage burnout indicated that the spin frequency during reentry was 8 rps.

In determining the orientation of a vehicle such as the Trailblazer, the possible influence of two types of precession must be considered. The first, an initial coning motion that could be induced by thrust deviations during the fourth-stage firing, would occur at a rate that can be calculated. The other, a coning motion externally induced by aerodynamic forces tending to realign the vehicle with the velocity axis, would occur only if the atmosphere were sufficiently dense.

To verify the presence of either or both precessions, an analysis of the flight data was carried out according to the methods of Caldecott et al (1967).

The axis associated with initial coning does not have to coincide with the spin or velocity vectors. The magnitude of any factors that might induce initial precession would affect only the relative position of the resulting precession axis—it would not affect the rate of precession. Any such precession would cause the angle of attack to exhibit a modulation corresponding to the precession rate. The parameters required to determine this rate are: I_T , the transverse moment of inertia of the nose cone; I_A , the longitudinal moment of inertia; and ω , the angular spin velocity.

For the case of the Trailblazer with a spin rate of 8 rps and the following values of the determining parameters:

$$I_T = 1.094 \text{ slug ft}^2,$$

$$I_A = 0.471 \text{ slug ft}^2,$$

$$\omega = 50.27 \text{ rad/sec},$$

the precession rate is

$$\phi = I_A \omega / I_T = 21.65 \text{ rad/sec} = 3.45 \text{ rps}.$$

The Trailblazer reentered at a nonzero angle. It was thus necessary to determine whether the initial precession, if any, was small enough to be neglected since it becomes difficult to determine a position for the vehicle axis if the vehicle is undergoing a precession of this nature. Two sets of data were examined: (1) the S-band antenna patterns, and (2) electron density values obtained with the electrostatic probes.

Nonuniformity in the antenna patterns causes variations in the received S-band signal strength. The presence of significant initial precession would have modulated the signal at the calculated 3.45 rps. No such modulation was apparent.

The electrostatic (ES) probes, which measure the electron density in the plasma over their respective locations, alternately record maxima and minima. The variation corresponds to the change in probe position resulting from the vehicle spin and angle of attack. If the vehicle is also undergoing other perturbations due to precession about some arbitrary axis, this would be apparent in the readings. Successive maximal (or minimal) levels would not be identical since the precession would induce cyclic variations. There was no evidence of this effect.

The overall spin and precession history reflected in the cyclic response of the ES probes is shown in Figure 14. Although there is no sign of initial precession, the probe data does clearly show precession of the vehicle about the velocity

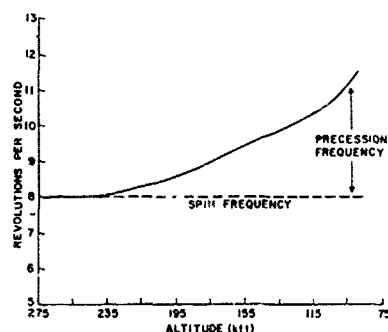


Figure 14. Electrostatic Probe Measurement of Spin and Precession

vector. At altitudes where the probes are affected by the presence of the plasma but where the atmospheric density is still relatively low, only the original spin rate is observable. There is no sign of aerodynamic precession until the vehicle is below 240 kft. At this point, precession begins to appear and its frequency continues to increase.

Two conclusions about vehicle precession can be drawn from the probe data. First, coning due to misalignment was not present or else was of such small magnitude that it had no noticeable effect on the sensors. Second, aerodynamic precession about the velocity vector became important only toward the end of the flight, and its effect was to shorten the time between maximal values of the electron density measured by the probes.

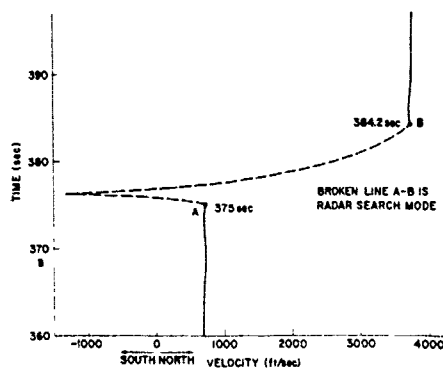
3.3 Angle of Attack

Since no indication of initial vehicle coning was present, the orientation of the vehicle during reentry can be specified. It is then possible to treat the payload spin axis as being aligned with the acceleration vector associated with the firing of the spherical motor. The vehicle angle of attack can then be determined by calculating the angle between the acceleration and velocity vectors.

A look at the history of the vehicle acceleration computed from the AN/FPQ-6 data for the north-south velocity component shows that the radar was unable to track the vehicle during the fourth-stage firing: the vehicle was lost at ignition and not regained until after burnout had occurred. Direct determination of the thrust direction was thus impossible. [In Figure 15, the broken line from point A (ignition) to point B (burnout) corresponds to the radar search mode rather than to the vehicle.]

To calculate the acceleration indirectly, the velocity components before and after firing were plotted. In each the separation between curves was taken to be proportional to the total acceleration in the respective component direction due to firing of the fourth stage. These magnitudes were then normalized to obtain the

Figure 15. North-South Velocity Component Before and After Fourth-Stage Firing



direction cosines for the acceleration vector. The velocity vector was also described by its direction cosines. Relating the two sets of direction cosines gave the angle of attack as 12.6° at burnout. On reentry the effect of gravity changed this angle to 12.8° .

For a reentry vehicle of the Trailblazer shape, the angle of attack in the non-spinning case begins decreasing at about 200 kft because of aerodynamic damping; by the time the vehicle drops to 130 kft, where aerodynamic stresses become severe, it is at a very small angle of attack. In the spinning case, however, aerodynamic damping at altitudes above 150 kft is negligible, and there is no alteration in the angle of attack except that due to gravity. In the present study, therefore, no change in the angle of attack had to be considered.

3.1 Antenna Polar Angle

Before analyzing the S-band antenna patterns received by the ground station, the polar field angle θ must be determined for the transmitting antenna at the stagnation point of the vehicle. Angle θ is defined as the angle between the longitudinal axis of the nose cone and its radius vector to the ground station (Figure B1, Appendix B). Since the vehicle is entering along an almost vertical path and the angle of attack is constant, angle θ will not change much over the altitude range of interest.

The direction cosines of the payload spin axis and of the velocity vector have already been determined. Converting the range and azimuth information contained in the analyzed data from the AN/FPQ-6 radar to vehicle-oriented coordinates yields the corresponding components of the slant-range vector and its direction cosines. The angle between the velocity vector of the nose cone and the vector to the ground station remains almost constant at 60° , and the polar angle θ for the antenna remains at about 45° , over an altitude range from 300 kft to 200 kft.

3.5 Flow Field Calculations

To compare theoretical models representing various electromagnetic phenomena with the experimental results requires knowledge of the environment surrounding the vehicle during reentry. Various techniques yielded electron densities, collision frequencies, and other flow properties for use with the theoretical models in describing the performance of the payload instrumentation.

The exact flow field description is extremely complex. The flight regime spans the altitude range from 300 kft to 150 kft, although some probe reading could still be obtained at lower altitudes. The vehicle has a spin rate of 8 fps and is at an angle of attack of about 12.5° over most of the flight. The result is a varying flow field history not easily represented by a simplified model. In consequence, individual calculations were done to provide the information required for analyzing each type of instrument reading. The range of methods to obtain results will be outlined and some typical examples given.

One difficulty was that many of the calculations were for altitudes well above 200 kft. In this regime the assumptions of a distinct thin boundary layer and an inviscid shock layer are invalid. At 250 kft and above, the flow has entered the merged layer condition where boundary layer effects could in some cases extend all the way to the shock. Since our approximate calculations do not provide for this, their applicability under such conditions is uncertain.

The plasma properties near the nose were of interest because of their effect on transmission from the S-band antenna. Somewhat extensive calculations of nonequilibrium electron density distributions in this region were therefore made.

Streamline regions in the nonequilibrium inviscid flow field around blunt bodies can be classified according to the chemical kinetics associated with them: those for which the dominant reactions are always binary, and those for which three-body recombination processes become important at some point.

The flow at the vehicle stagnation point is considered to be in thermochemical equilibrium. To satisfy this condition the nonequilibrium flow along the stagnation streamline must undergo recombination in the low-velocity reaction zone adjacent to this point. Since three-body reactions are present in this zone, a solution requiring binary kinetics criteria cannot be applied to the stagnation streamline in general; however, if care is taken to exclude the recombination region, the remainder of the streamline is amenable to solution by such an analysis.

The flow history for binary reaction regions is controlled by the quantity $\rho_\infty r_b$, the so-called binary scaling parameter, where ρ_∞ is the freestream density and r_b is the body radius. This indicates that when only binary processes dominate, nonequilibrium effects can be scaled as a function of the body size and the freestream density. Thus, for a given reentry velocity, the nonequilibrium

patterns displayed by a small body at one altitude can be considered to be similar to those displayed by a larger body at a correspondingly higher altitude. This approach was adopted in the present case so as to include some nonequilibrium chemistry effects in describing the flow around the vehicle nose.

Several assumptions and approximations were made in arriving at the solution. For one, the overall distribution of chemical species for the non-equilibrium solution was assumed to give a density that is of the same order as the equilibrium result. The detachment distance could then be considered to be approximated by the corresponding equilibrium value. [It should be noted that the use of nonequilibrium solutions introduces high-temperature effects near the shock, which would not ordinarily be present in an equilibrium result.]

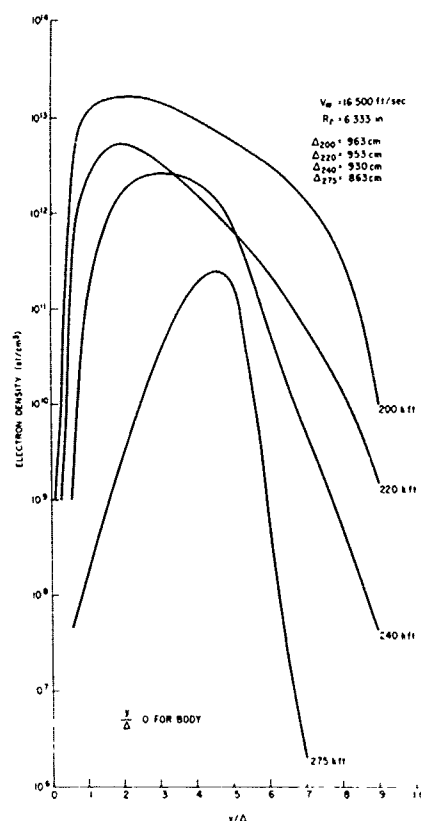
The scaling could not be applied near the stagnation point so the curves had to be faired-in to match the equilibrium stagnation values. At some altitudes the electron density distribution exhibited an overshoot near the vehicle, thus complicating the matching process.

Curtis, Burke, and Hayman's (1963) curves of stagnation-region electron density distributions for a hemisphere nose cone having a velocity of 16,500 fps were used, and the results were mapped to the inviscid stagnation region of the Trailblazer by the binary scaling parameter. The calculations were performed for a number of cases for the altitudes from 200 kft to 275 kft.

The inviscid shock-layer results were matched to boundary-layer properties. Inasmuch as it has already been indicated that any theory of thin nonmerged boundary layers was questionable under the flight conditions of interest, only the simplest order-of-magnitude type of calculation was used. Locally similar boundary layer equilibrium solutions for the stagnation region were assumed to hold. Nerem's (1962) procedures were used to obtain approximations to the properties and the layer thickness.

A better approximation to the actual flow was obtained through graphical merging of the inviscid and boundary layer results, with the merging performed so as to favor inviscid results in the outer region and boundary layer properties near the body. High temperatures near the shock showed that the collision frequency in that area must be modified. Since the temperature and density remain fairly constant over a large part of the outer boundary layer, the collision frequency in that part of the flow must also be relatively constant. The final form of the solution included these features. Figure 16 shows the electron density distributions as a function of altitude. This approach is most likely valid at only the lower altitudes; at the higher altitudes it is even possible that the thickness of the shockfront itself may introduce further viscous uncertainties into the already complicated picture.

Figure 16. Electron Density Profiles in the Stagnation Region



The computer program for analyzing antenna transmission required inputs for the distributions of electron density n_e and collision frequency ν . The distributions were broken down into several slabs, and an average value for n_e and for ν was assigned to each slab (Appendix A). A cool air layer was included at the body surface. The calculated stagnation region properties were taken to be the ones seen by the nose antenna.

The electrostatic and electroacoustic probes were located at various points around the body. These probes measured only the properties in the boundary layer. For the points located on the flank of the vehicle, flat-plate calculations for the boundary layer thickness were used. The outer edge of the boundary layer was taken as the stagnation streamline. Properties along this streamtube were calculated from assumed body pressure distributions and the normal shock entropy, which was assumed to be constant around the body.

The electron density and collision frequency distributions around the body are seen in Figure 17. In the input to various calculations, the electron density was assumed to be constant over the outer 0.6 thickness of the boundary layer profile, followed by an exponential dropoff toward the vehicle surface. It is

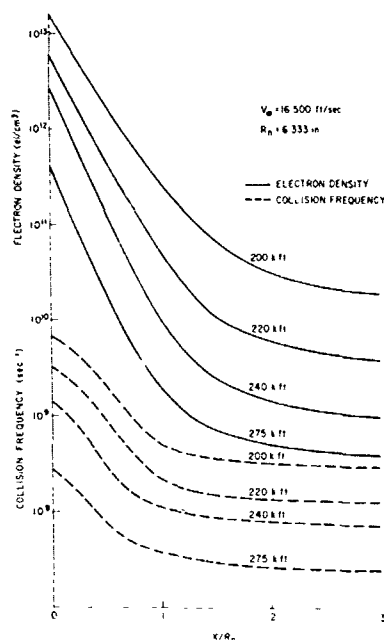


Figure 17. Stagnation Streamline Electron Density and Collision Frequency Distributions Around the Body

recognized that such results tend to be inaccurate; nevertheless, they can at least serve as some guide to theoretical predictions for the various probes.

In connection with the probe analysis, there is one further set of flow field data. The electrostatic probe results were studied both here and at Stanford Research Institute. As part of their probe study, SRI used some approximate flow properties to get results in a form that could be compared with the flight data. Their calculations are discussed in detail in Sec. 4.3.

4. PROBE THEORY AND RESULTS

The two types of plasma probes included in the Trailblazer payload are physically described in Sec. 2.3. One was a conventional flushmounted electrostatic (ES) probe developed by the Stanford Research Institute. The other, a new type of device that uses the properties of longitudinal plasma waves for probing the plasma sheath, was an electroacoustic (EA) probe developed at the Sperry Rand Research Center. The flight test results show the EA probe to be a most valuable device for probing properties in the boundary layer of the reentry plasma sheath.

The EA probe measures plasma properties only at discrete altitudes since it depends on resonance conditions being present in the reentry sheath. The ES probe output is continuous, the useful information from this probe being dependent

only on the rate at which the probe output is sampled. The electron density n_e at a particular point r_s in the sheath can be calculated from the output of the ES probe. The electron density n_e and its gradient n'_e at some other point r_o in the plasma sheath can be determined from the EA probe resonances. A direct measurement of the electron density gradient was previously not possible.

Probe operation and theory is discussed in Secs. 4.1 and 4.2. The results obtained from reduction of the probe data are presented in Secs. 4.3 to 4.5.

4.1 Electrostatic Probe Theory

The electrostatic probe discussed here is simply a circular conductor (see Figure 11). It consists of a 0.25-in.-diam. iridium-plated molybdenum electrode flushmounted on the reentry nose cone and electrically isolated from the vehicle skin by a ring of boron nitride dielectric. In order to provide data over a wide dynamic range the probe works into a logarithmic amplifier.

On the face of it, the ES probe appears to be the simplest device for probing the macroscopic properties of a plasma since it is only an isolated electrode used with a dc power supply and ammeter. Actually, the probe constitutes a boundary, and the equations that describe the plasma must be greatly changed in character to deal with conditions in the vicinity of a boundary, as in the case of the wall of a discharge tube. The electrons, whose mobility is much greater than that of the positive ions, tend to migrate to the wall much faster than the positive ions do, and so a sheath of electrons is formed at the wall. The resulting space charge decreases the electron current to the wall until it is equal to the positive current. This creation of a sheath region where charge neutrality is not present thus maintains charge neutrality in the bulk of the plasma.

The thickness of the sheath is on the order of a Debye length $\lambda_D = (kT_e/4\pi n_e)^{1/2}$. This would also be the thickness of the sheath formed over an isolated plasma probe. If the probe is biased relative to the potential assumed by an isolated probe (termed the floating potential), the sheath thickness is given approximately by

$$d_s \approx \lambda_D \eta^{3/4}, \quad (1)$$

where $\eta = |eV/kT_e|$, and V is the probe bias voltage.

To determine the properties of the plasma from the output of the probe requires an analysis of the sheath region. This complicates an otherwise simple diagnostic system. If the probe size and mean free path λ_m in the plasma are much greater than the Debye length, conventional probe theory is valid and can adequately describe the probe data. For instance, if the probe is biased increasingly positive with respect to the floating potential, the number of positive ions reaching the probe will

decrease until only electrons are collected. Under this condition of electron saturation, collisionless probe theory (Chen, 1965) results in the equation

$$j_e = \frac{n_e e v_e}{4} \quad (2)$$

for the relationship between the saturated electron current density j_e and the electron density n_e , where v_e is the electron thermal velocity, and e is the electron charge.

If the probe is biased negative enough with respect to the floating potential, only positive ions are collected. For the saturated ion current density, the theory of Bohm, Burhop, and Massey (1949) gives

$$j_i = \frac{1}{2} n_i e \left(\frac{k T_e}{M} \right)^{1/2}, \quad (3)$$

where k is Boltzmann's constant, T_e is the electron temperature, and M is the ion mass.

In addition, the probe can be operated in the region between ion and electron saturation. When collisionless theory is applicable, the electron temperature can easily be obtained from the probe current-voltage characteristic in this region.

For $\lambda_m < \lambda_D$, however, collisionless theory does not hold, and probe analysis becomes much more difficult. Electrostatic probes flushmounted on a hypervelocity reentry vehicle present an even more complicated problem in probe analysis. The theory of current collection by surface electrodes through boundary layers is not yet well enough understood.

An inhomogeneous plasma layer is formed around the vehicle. From a low value close to the vehicle surface, the electron density increases to a maximum at the edge of the boundary layer and then decreases with distance into the laminar flow region. The low electron density close to the vehicle surface results in a large Debye length in this region. In general, this means that the mean free path is less than the sheath thickness so the effects of collisions in the sheath must be included in the analysis. Also, if the probe bias is high the plasma sheath will extend far enough into the boundary layer to require including the effect of convection in the analysis.

Two theoretical treatments of this problem predict the probe current-voltage relation in simple analytic form. Chung and Blankenship (1966) analyzed the operation of a double probe system in which the two isolated electrodes of the probe are located on opposite parallel plates between which the hypersonic ionized air flows. In their analysis, electron-ion recombination is considered to be frozen and it is

assumed that either the electron temperature is in equilibrium with the neutral gas temperature or the collisional equilibration process between the electron and neutral gas temperatures is frozen. The mean freepath for electron-neutral collisions is assumed to be smaller than any other effective length in the problem. The neutral gas boundary-layer solutions yielding velocity and neutral gas temperatures profiles are considered to be known throughout the flow field. This of course assumes a decoupling between the neutral and ionized gas flows, and is justified so long as the degree of ionization is low (<1 percent). The boundary layer is divided into sheath and ambipolar regions. Then, for the case of electron-neutral gas temperature equilibration, the number density conservation equations for ionized species and Poisson's equation are solved in both these regions and also in the inviscid flow region. When the electron temperature is not equal to the gas temperature the electron energy conservation equation must be added to the system of equations. Since these equations include an assumed linear relationship between the probe electric field and the drift velocity attained by the ionized species, validity of the theory is limited to low values of the quantity $\eta = |eV/kT_e|$, where η is the ratio of the energy gained from the field to the thermal energy of the ionized species.

[Some SRI (Scharfman and Bredfeldt, 1967) experimental work on flush-mounted electrostatic probes has shown that the assumption of linear mobility coefficients breaks down for probe biases much above 15 V. The SRI tests were conducted in an air-filled shock tube for ambient pressures of 0.1 and 1 Torr, and electron densities in the range from 10^8 to $10^{14}/\text{cm}^3$.]

The Chung and Blankenship solutions for the equation in each region are matched at the boundaries and a numerical analysis is made to obtain potential-current characteristics for the probe system. This analysis shows that there is a saturation current, that is, a region where current is independent of voltage. For this region the following simple analytic formula is obtained, relating charged-particle density at the edge of the boundary layer to the flow field properties in the boundary layer and the current drawn by the probe:

$$qn_{e,\infty} = \frac{2^{3/2} \left(\frac{x_2}{U_\infty \nu_\infty} \right)^{1/2} (j_e - j_i)}{1 + 0.94 (T_e/T_g)_\infty} \quad (4)$$

In this expression, x_2 is the distance from the leading edge of the plate, U_∞ is the velocity at the edge of the boundary layer, ν_∞ is the kinematic viscosity at the edge of the boundary layer, $(T_e/T_g)_\infty$ is the ratio of electron temperature to gas temperature at the edge of the boundary layer, $(j_e - j_i)$ is the net current to one electrode, and q is the particle charge.

In another, much simpler, treatment of this problem for higher values of η , Scharfman and Bredfeldt of SRI (1967) assume planar geometry and no recombination or ionization in the sheath. The energy gained by an ion within the first mean free path is assumed to be large enough so that scattering tends forward in the subsequent collision and very few ions are scattered out of the sheath. The current collected is therefore set equal to the full random current that is at the sheath edge and moving in the direction of the probe. Hence,

$$j_i = \frac{1}{4} n_{is} e (v_{is}) , \quad (5)$$

where n_{is} is the ion density at the sheath edge, and v_{is} is the ion thermal velocity at the sheath edge.

To locate the edge of the sheath in the SRI treatment, it is assumed that the charge redistributes itself within the sheath such that the current at the probe is governed by the same relationship as in the case of a mobility-controlled space-charge-limited diode, where

$$j_i = \frac{9}{8} \epsilon_0 \mu_{is} \left(\frac{V^2}{r_s^3} \right) , \quad (6)$$

with ϵ_0 the permittivity of freespace, μ_{is} the mobility at the sheath edge, r_s the distance of the sheath edge from the probe, and V the probe bias voltage.

4.2 Electroacoustic Probe Theory

Operation of the EA probe depends on the possibility of exciting longitudinal electromagnetic waves that under certain conditions resonate between a point in the plasma sheath and the reentry vehicle surface. The development of a probe unit making use of this phenomenon to measure properties of the plasma sheath during reentry was suggested by Schmitt (1964) of the Sperry Rand Research Center. The basic feasibility studies and development of the probe unit were performed by Sperry Rand under contract (Lustig and McBee, 1969).

The resonant excitation of longitudinal waves in an inhomogeneous plasma can be observed in the resonant scattering or absorption of continuous electromagnetic waves from a plasma column. The effect was first noticed by Tonks in 1931. Detailed study of the phenomenon began with the work of Dattner in 1957. The phenomenon is commonly referred to in the literature as Tonks-Dattner resonances.

At present, the frequency spectrum of the resonances is quite adequately predicted by the continuum theory for a warm plasma. To determine fine structure such as line shape requires a microscopic theory because the dominant broadening mechanism is Landau damping, a collisionless form of damping that cannot be predicted by continuum theory.

For the discussion in this section it will suffice to consider only the continuum theory. We can picture the resonance as arising from the excitation of electroacoustic waves in the plasma close to the boundary (Figure 18), where the frequency of the wave ω is higher than the local plasma frequency ω_p . These electroacoustic waves are longitudinal electron oscillations whose restoring force is electrostatic. For the case of an infinite homogeneous plasma the dispersion relation between the wave number K and the wave frequency ω is

$$K^2 = \frac{\omega^2}{\omega_p^2} \left(\frac{\omega^2 - \omega_p^2}{3 \frac{kT_e}{m_e}} \right), \quad (7)$$

where $\omega_p = [n_e^2 / (\epsilon_0 m_e)]^{1/2}$, k is Boltzmann's constant, T_e the electron temperature, and m_e the electron mass. These waves propagate with a phase velocity on the order of the electron thermal velocity $v_T = (kT_e / m_e)^{1/2}$. Their wavelength is much shorter than the corresponding freespace wavelength.

Electroacoustic waves will not propagate in regions where their frequency is lower than the plasma frequency. An electroacoustic wave propagating toward an overdense region (where $\omega < \omega_p$) will be reflected at the point in the plasma where $\omega = \omega_p$. It will also be reflected in the vicinity of metal boundaries such as the reentry vehicle skin.

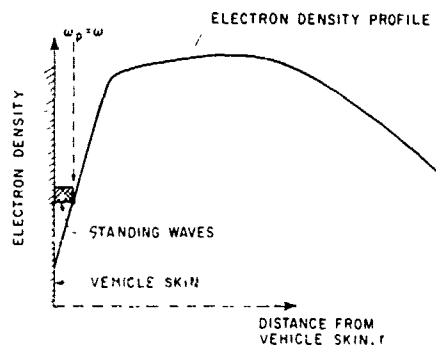


Figure 18. Electron Density Profile in Plasma Sheath Showing Region Where Electroacoustic Resonances Are Excited

Assume an electroacoustic wave to be excited near the boundary of the sheath, with r the distance from the boundary, and ω greater than the local plasma frequency $\omega_p(r)$ but less than the maximum plasma frequency ω_{pmax} in the sheath. The wave will propagate and be reflected at the point $\omega = \omega_p(r_0)$. If the total phase shift when the wave returns to the vicinity of the boundary is any multiple of 2π it sets up a standing wave, and the plasma structure will be in resonance with the excitation mechanism.

Application of continuum theory results in a third-order differential equation for the propagation of electroacoustic waves in an inhomogeneous plasma. This equation will predict the resonant condition only through numerical analysis; however, for the lower-order resonances, a WKB type of analysis appears to be valid. Assuming a cosine density profile:

$$\frac{e^2 n_e(r)}{\epsilon_0 m_e} = \omega_p^2(r) = \omega_{pmax}^2 \cos \frac{\pi}{2} \frac{r}{a}, \quad (8)$$

we obtain the resonance condition relating frequency and the plasma density gradient, which is

$$\frac{\omega_{pmax}^2}{a} = \frac{2}{\pi \left(\frac{3kT_e}{m_e} \right)^{1/2}} \frac{\omega^3}{(\gamma - 1/4)}, \quad (9)$$

where γ , the order of the resonance, takes on only integer values 1, 2, ... the point r_0 in the sheath where $\omega^2 = \omega_p^2(r_0) = \omega_{pmax}^2(r_0/a)$ is given by

$$r_0 = \frac{\pi}{2} \left(\frac{3kT_e}{m_e} \right)^{1/2} \left(\gamma - 1/4 \right) \left(\frac{1}{\omega} \right). \quad (10)$$

The results obtained by using the WKB approximation were compared with the results obtained by numerical analysis from a more complete theory developed by Ewald (1968). Agreement was adequate (to within 20 percent) for the first three resonances.

Sperry Rand experiments showed that it is possible for a planar open-ended coaxial line located outside a discharge tube to couple strongly to electroacoustic waves. The same type of transducer (Figure 10) was chosen for our reentry experiment. The geometry of the device makes it possible to flushmount it on the reentry vehicle so that it does not interfere with the gaseous flow fields around the

vehicle. In the absence of a plasma the transducer is a weak radiator since its dimensions are small compared with the freespace wavelength. Under this condition, almost all the power is reflected. Sperry Rand's experimental work showed there is a power reflection of about 30 percent at the center of the first resonance ($\gamma = 1$). Thus, for the transducer to be used as a flight instrument for detecting resonance, only the reflected power needs to be monitored. The required detection system is a simple reflectometer whose circuit is shown in Figure 9.

Before ending this discussion of EA probe characteristics it is necessary to consider one assumption that has been made but not explicitly stated. This is that electroacoustic wave-damping through electron-neutral collisions is small enough to be neglected. For the damping to be this small, the electron collision frequency ν must be small compared with the wave frequency.

Experimental work by Sperry Rand showed that if $\nu = \omega/2\pi$, the first three resonances can be observed. The frequencies for the flight test were therefore chosen such that ω would be greater than the collision frequency ν in the plasma sheath when conditions favorable to observation of the first three resonances were present. [Observation of three resonances would guarantee proper identification of the resonances.] Subsequent experimental work at Sperry Rand showed, however, that $\nu < \omega/2\pi$ is not a sufficient condition for observing the first three resonances.

The intensity of electroacoustic resonances as a function of gas pressure (proportional to electron-neutral collision frequency) for an air afterglow plasma is plotted in Figure 19. It can be seen that as the collision frequency increases,

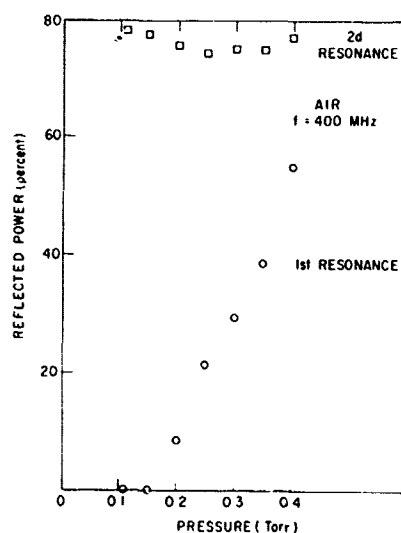


Figure 19. Intensity of Electroacoustic Resonances Versus Gas Pressure

the resonances decrease in intensity and merge together—as is to be expected—but that as the collision frequency decreases, the second and third resonances decrease in intensity while the first resonance remains constant. There is at the moment no explanation for this behavior. The reentry flight data seems to show the presence of this effect.

4.3 Electrostatic Probe Results

Usable data was obtained only from ES probes Nos. 2 and 3, respectively located at $S/R_n = 1.31$ and $S/R_n = 2.72$ (Figure 4). Probe No. 1, located nearest the stagnation point, read almost constant current long before reentry and down through reentry, indicating that something was wrong with the probe channel.

The measured values of the ES probe currents obtained from probes Nos. 2 and 3 were reduced to values of electron density according to the theories of both Chung and Blankenship and of Scharfman and Bredfeldt (SRI) that were discussed in Sec. 4.1. The Chung theory yields the value of the electron density at the edge of the boundary layer; the SRI theory yields the value of the electron density at some other point within the boundary layer.

These theories do not both have the same range of applicability. In the SRI series of experiments to study operation of the flushmounted ES probe, a shock tube was used to simulate flow field conditions found about a hypervelocity reentry vehicle. The test gas was air, and both 0.1 and 1.0 Torr initial shock-tube pressures were used. In equating ambient gas density behind the shock to simulate altitude, 0.1 Torr represented 150 kft, and 1.0 Torr represented 100 kft. Freestream charge densities in the range from 10^9 to 10^{14} e/cm³ were produced. The ES probe was flushmounted on a flat plate located in the shock tube and biased -3V, -15V, and -90V to collect positive ions.

Chung's theory (see Sec. 4.1) contains the assumption of a linear relationship between ion velocity and the applied electric field. This implies that the average energy that an ion gains from the field in one mean free path is much smaller than the ionic thermal energy, that is, $\eta = |eV/kT_e| \ll 1$. Further assumptions are continuum flow, chemically frozen boundary layer, and sheath thickness small relative to the boundary-layer thickness. The theory predicts that the ion current saturates above a certain voltage.

On the other hand, the SRI theory assumes that the average energy that an ion gains in the first mean free path within the sheath is much greater than the ionic thermal energy, that is, $\eta \gg 1$. Under this assumption the full random ion current is collected from the sheath edge. The sheath edge is assumed to be given by the planar, space-charge-limited, mobility-controlled diode equation, which contradicts Chung's theory in that it predicts that collected current is a function of probe bias.

Allowing these assumptions, Chung's theory should apply at low values of probe bias and the SRI theory should apply at higher values of probe bias. The shock tube studies conducted at SRI bear this out. At a probe bias of -3 V , Chung's theory gives a better fit to the experimental data; at -90 V the SRI theory gives a better fit. At -15 V , the bias used on the reentry test, the predictions of each theory bound the experimental data. The SRI theory underestimates the charge density at the edge of the boundary layer by about a factor of 2, whereas the Chung theory overestimates it by the same amount. Since this is within the limits of accuracy of the flight test, both theories can be applied to reduce the data.

A sample of the raw data obtained by ES probe No. 3 is shown in Figure 20. The modulation of the probe current is due to the nonzero angle of attack assumed by the vehicle as it reentered the atmosphere spinning about its longitudinal axis. This initial angle of attack caused asymmetries in the electron density distribution in the plasma sheath, about the longitudinal axis of the nose cone. The ES probe data was used to determine the apparent change in spin rate due to precession of the nose cone caused by aerodynamic drag (See Sec. 3.2).

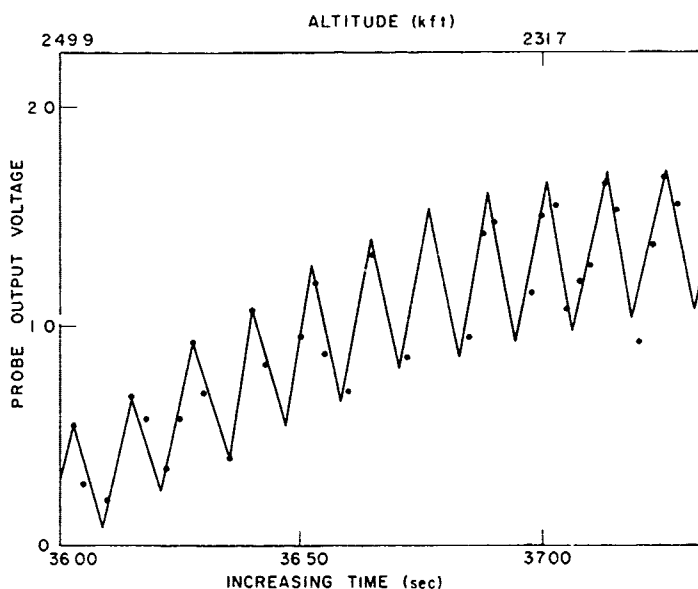


Figure 20. Voltage Measured by Electrostatic Probe No. 3 ($S/R_n = 2.72$) Versus Altitude

The ES probe data was reduced by SRI, using the Chung theory. For singly charged ions, Eq. (4) becomes

$$n_{e, \infty} \left(\frac{\text{ions}}{\text{cm}^3} \right) = 9 \times 10^{12} j_i \left(\frac{x_2}{U_{\infty} \nu_{\infty}} \right)^{1/2}. \quad (11)$$

From a report by Evans and Huber (1963), which presented values of flow field parameters for an altitude of 170 kft, the following values were obtained:

$$U_{\infty} \approx 11 \text{ kft/sec}$$

$$T \approx 4000^\circ \text{K},$$

$$\rho/\rho_0 \begin{cases} \approx 7 \times 10^{-4} \text{ for } S/R_n = 1.31, \\ \approx 4.5 \times 10^{-4} \text{ for } S/R_n = 2.72, \end{cases}$$

where ρ/ρ_0 is the ratio of air density at the edge of the boundary layer to that at sea level. At 170 kft, the ratio of the ambient air density to that at sea level is approximately 7×10^{-4} . Therefore, at probe No. 2, $\rho_{\infty} \approx \rho_{\text{amb}}$, and at probe No. 3, $\rho_{\infty} \approx 0.64 \rho_{\text{amb}}$. At the stagnation point, $\rho_{\infty}/\rho_{\text{amb}} \approx 14$. It was assumed that the ratio of $\rho_{\infty}/\rho_{\text{amb}}$ for each station was the same at all altitudes.

Values of dynamic viscosity μ , obtained from tables for the side of the vehicle and the stagnation point, were

$$\mu \begin{cases} = 8.75 \times 10^{-4} \text{ gm/cm sec (side)} \\ = 10^{-3} \text{ gm/cm sec (stagnation point)}. \end{cases}$$

The relationship between the kinematic viscosity ν and the dynamic viscosity μ is $\nu = \mu/\rho$.

The results of interpreting the probe currents in this manner are shown in Figures 21(a) and (b), which give only the envelopes of the ES probe data. The maximum value of the electron density at any altitude is read when the ES probe is sampling on the windward side of the vehicle. The minimum values are obtained when the probe is on the leeward side of the vehicle.

The figures include the equilibrium values of electron density computed by Hartsel and Nerem (1964) of Ohio State University. Their frozen values are more than an order of magnitude higher than the equilibrium values. The equilibrium values for $S/R_n = 1.31$ and 2.72 were obtained from the OSU report by adjusting the computed value at $S/R_n = 1.57$ upward by a factor of 2 for $S/R_n = 1.31$ and downward by a factor of 2.5 for $S/R_n = 2.72$. These adjustments are in accord

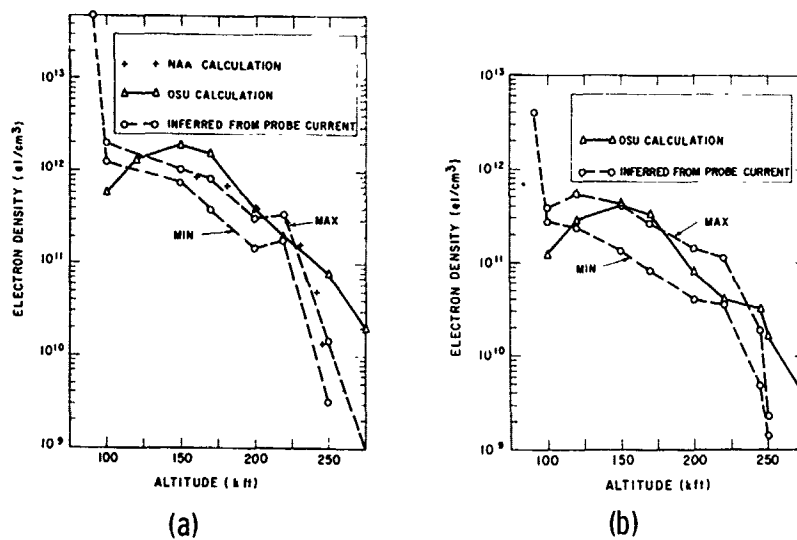


Figure 21. Electron Density at Edge of Boundary Layer Versus Altitude [(a) electrostatic probe No. 2 ($S/R_n = 1.31$), (b) electrostatic probe No. 3 ($S/R_n = 2.72$)]

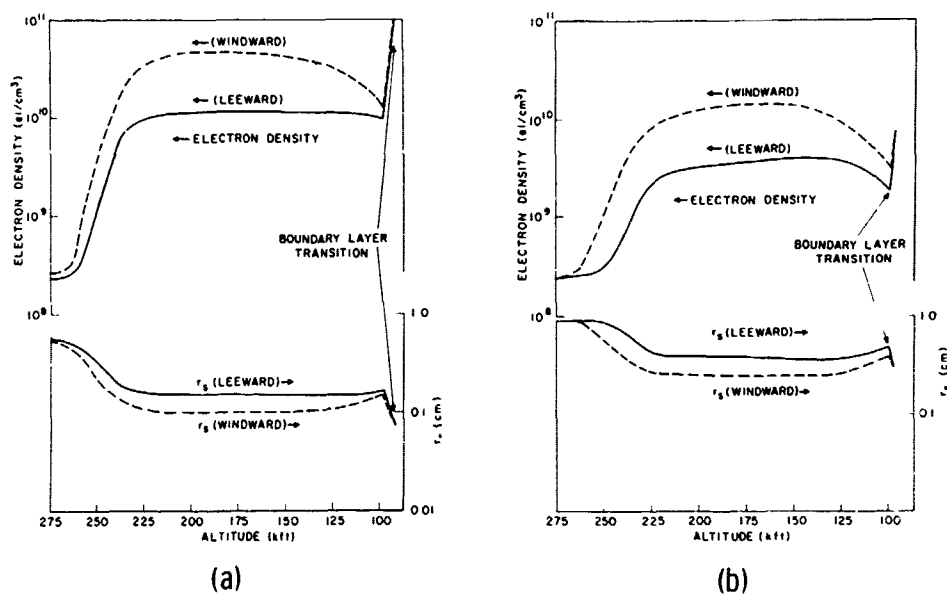


Figure 22. Electron Density at Separation of r_s From Vehicle Surface Versus Altitude [(a) electrostatic probe No. 2 ($S/R_n = 1.31$), (b) electrostatic probe No. 3 ($S/R_n = 2.72$)]

with the variation along a streamline shown in the OSU report for an altitude of 170 kft. In other words, it is assumed that the ratio of the equilibrium electron density at $S/R_n = 1.57$ to that at the probe locations is constant throughout the entire altitude range.

An examination of the figures shows that above 230 kft the probes indicated an electron density significantly lower than equilibrium. This is probably due to inadequacy of the flow field calculations at high altitudes.

Some modified continuum flow field calculations, made for the NASA RAM B-3 vehicle by Ball et al of North American Aviation (1965), can be applied to interpret the data from ES probe No. 2. The RAM B-3 vehicle is similar in shape to the Trailblazer, having a hemisphere nose cap of 4-in. radius and a 9° cone afterbody. The NAA solution allows the boundary layer to interact with the inviscid flow. The initial boundary layer thickness that is used to give an effective body shape leads to altered outer edge properties that in turn determine a new viscous solution. Inviscid streamlines are incorporated into the boundary layer as they intersect the outer edge location around the body. The two regions are each modified to include non-equilibrium effects and the final profiles are faired together, producing a single overall distribution of properties from the body to the shock. Calculations for a reentry velocity of 17.5 kft/sec were made at a RAM B-3 vehicle station of $S/R_n = 1.25$ (which roughly corresponds to the position of ES probe No. 2). The NAA values of the electron density at the edge of the boundary layer were dropped by a factor of 2 to account for the 1 kft/sec slower reentry velocity of the Trailblazer vehicle. These results are also shown in Figure 21(a). The numerical agreement with the probe results is gratifying, but even more important is the agreement between the predicted sharp drop in electron density above 230 kft and the measured result.

The data from ES probes Nos. 2 and 3 for altitudes below 100 kft indicates that boundary-layer transition—that is, laminar-to-turbulent flow—occurred at about 96 kft, marked by a rapid increase in probe current. Probe No. 3 showed an increase in current before probe No. 2 did as the transition moved forward along the body.

Figures 22(a) and (b) show the results of reducing the data from ES probes Nos. 2 and 3 according to the theory of Scharfman and Bredfeldt (SRI). The electron density n_e at a point in the boundary layer, and the separation of this point from the surface of the vehicle (r_s), are plotted in these figures. Since typical values of the boundary layer thickness are 1 cm at the position of ES probe No. 2, and 4 cm at ES probe No. 3, it is clear that the value of r_s is only a small fraction of the boundary layer thickness over most of the altitude range. It is therefore probably a fair approximation to assume a linear variation in electron density from the vehicle surface out to point r_s . The value of the ratio n_e/r_s

would thus represent a good estimate of the electron density gradient close to the vehicle surface.

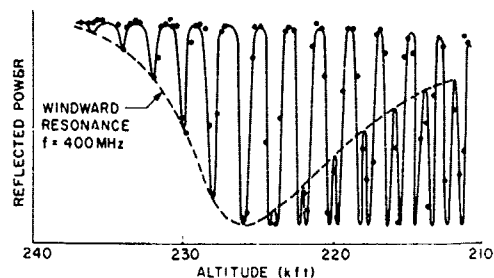
Our analysis of the EA probe data (Sec. 4.4) shows that the point in the plasma sampled by the EA probe lies close to the sheath edge predicted by the SRI theory. The ES data analyzed by the SRI theory can thus be used as a cross check on the operation of the EA probe.

4.4 Electroacoustic Probe Results

Valid data was obtained from the 1500-MHz probe located at $S/R_n = 0.7$ and from one of the 400-MHz probes located at $S/R_n = 2.72$. Owing to an equipment malfunction the other 400-MHz probe gave only a weak return but it did show a weak resonance while the other 400-MHz probe was showing a strong resonance. The 100-MHz probe was included only as backup in case it turned out that the estimates of flow field quantities, upon which the 400-MHz probe was selected, had been greatly overestimated. For 100 MHz the sensing area of the probe had to be made larger than that used for the higher frequencies. This probably made the 100-MHz probe more sensitive to interference from the S-band transmissions and accounted for the irregularity in the data that was obtained.

Typical electroacoustic probe data is shown in Figure 23. The resonance shown is the envelope of a more rapidly varying response caused by the spin of the vehicle and the nonzero angle of attack. Because of the nonzero angle of attack, the stagnation point is displaced from the centerline of the vehicle and a precession about the velocity vector results from the aerodynamic drag. Flow field parameters are thus not symmetric about the center axis, and in its rotation about the body axis the probe sees different plasma conditions. The electron density is greatest when the probe is sensing closest to the stagnation region (windward side) and least when sensing is furthest from the stagnation region (leeward side).

Figure 23. Reflected Power Versus Altitude for 400-MHz Electroacoustic Probe ($S/R_n = 2.72$)



Four time periods determine the shape of the observed signal from the EA probe. They are: τ_r , duration of one revolution of the vehicle about the body axis; τ_w , lifetime of resonance, dependent on damping mechanisms; τ_{ne} , time span during reentry, when the electron density is changing rapidly; and τ_p , precession about the velocity vector.

The modulation rate of the ES and EA probe data is due to the spin about the vehicle axis and precession about the velocity vector. Examination of the ES data shows that the modulation rate increased as the altitude decreased. The precession was therefore opposite in sense to the spin. The vehicle was spinning clockwise about its axis. The data thus shows that it was precessing counter clockwise about the velocity vector. The data also shows that the precession rate first became appreciable below 170 kft. This is well below the altitude range where the rapid buildup in electron density took place. The time period for precession τ_p may therefore be considered to be much longer than the other three periods and plays no role in the analysis. The modulation of the ES probe data during the time of plasma buildup shows that

$$\tau_r \ll \tau_{ne}.$$

If we had $\tau_w \ll \tau_r$, we would have the ideal situation where the probe response is of the following form. First, a narrow resonance appears on the windward side. Since the plasma condition necessary for resonance exists on both sides of the windward generatrix, two resonances occur on the next revolution. On succeeding revolutions these two resonances move further and further away from the windward side until they merge to form one resonance on the leeward side and then disappear. When plasma conditions are such that a higher-order resonance is observed on the windward side, the process begins anew.

This ideal situation is not what was observed during the flight test. In Figure 23 we see the appearance of a resonance, followed by a complicated oscillatory structure, after which the resonance disappears. The probe response remains relatively constant during the rest of the flight. In the case of the EA probe the resonance region first appears at about 250 kft and disappears at 210 kft. In the data from EA probe No. 4 the resonance region appears at 235 kft and is evident down to 160 kft.

This behavior indicates that τ_w is not much shorter than all other time constants. Since the resonance region lasts about as long as τ_{ne} it must be assumed that

$$\tau_w \approx \tau_{ne}.$$

The ES probe data yielded time markers for determining when the probes were sensing on the windward side and when they were sensing on the leeward side. Using these markers for the resonance region, for EA probe No. 1 we found a resonance on the windward side at the beginning of the region, and a resonance on the leeward side at the end of the region, as would be expected. For EA probe No. 4 we also found a resonance on the windward side at the beginning of the resonance region, and a very broad and weaker response on the leeward side. Here, in all probability, plasma conditions were not changing rapidly and the probe was operating on one side of the resonance. The data was not fine-grained enough to follow the resonances as they moved around both sides of the vehicle toward the leeward side. It was, however, possible to observe this effect taking place: right after a full resonance condition was achieved on the windward side, the probe response began to increase again at the next windward time marker but, on both sides of the windward time marker, the probe response remained at its low resonance value.

The 1500-MHz probe indicated the same resonance on the windward side at 240 kft as on the leeward side at 220 kft. The 400-MHz probe indicated resonance on the windward side at 220 kft, but the broad and weak response observed on its leeward side was not indicative of a full resonance.

To ensure proper labeling of each resonance, the frequencies had been selected such that at least three resonances would be observed (Sec. 4.2). Only one strong resonance, however, was observed by each probe. This seems to indicate that collision frequencies were smaller than anticipated, with only the lowest-order resonance observed.

Table 1 lists the values of the plasma sheath parameters, determined from Eqs. (9) and (10), that will yield the lowest-order ($\gamma = 1$) resonance.

Table 1. Plasma Parameters for Electroacoustic Resonance

Freq. (MHz)	T_e (°K)	r_o (mm)	$n_e(r_o)$ (el/cm ³)	$[n_e(r_o)]/r_o$ (el/cm ³ /cm)
1500	2500	0.10	3×10^{10}	3.3×10^{12}
400	1000	0.20	2×10^9	9.7×10^{10}

The values for the electron temperature T_e were based on a theoretical calculation of the electron temperature profile in the boundary layer (Hartsel and Nerem, 1964). The estimate of T_e is not critical to the calculation since T_e is included in Eqs. (9) and (10) as $(T_e)^{1/2}$.

4.5 Comparison of EA and ES Results

Figures 24 show the sheath electron density profile indicated by (a) the 1500-MHz and (b) the 400-MHz probe results. The electron densities obtained from the ES probe data using the SRI theory are also shown. Since no ES probe was located at the same station as the 1500-MHz EA probe, the density measured by ES probe No. 2 located further back on the vehicle was scaled up by the ratios of the predicted equilibrium electron densities based on flow field calculations. Shock tube studies at SRI show that their theory underestimates the actual electron density by a factor of from 2 to 4. In the light of this result, the agreement between the EA and ES probe results is quite adequate.

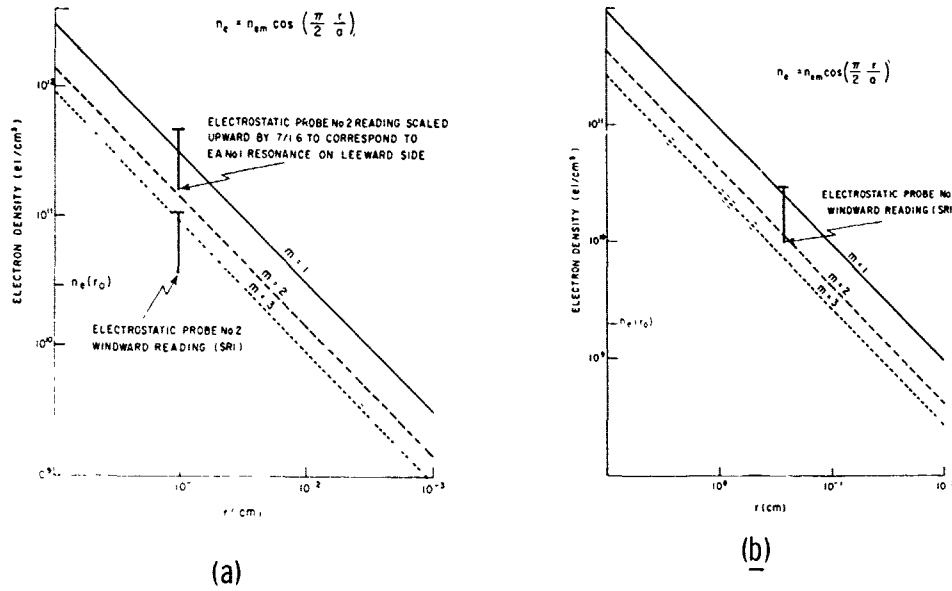


Figure 24. Electron Density Profile Measured by (a) the 1500-MHz Electroacoustic Probe No. 1 ($S/R_n = 0.7$); (b) the 400-MHz Electroacoustic Probe No. 4 ($S/R_n = 2.72$)

5. S-BAND SLOT ANTENNA STUDIES

5.1 Antenna Admittance and Coupling

A major objective in this flight test program was to obtain measurements of the influence of the reentry plasma sheath on the performance of an S-band slot antenna at both high and low power levels. Owing to erratic behavior of the S-band transmitter, the high-power measurements were equivocal. This report therefore discusses only the low-power signal (linear) effects of the microwave-plasma interactions, including the influence of the plasma sheath on the transmitting antenna's terminal admittance (mismatch), interantenna coupling, signal attenuation, and pattern distortion.

The S-band transmitting antenna is a dielectric-filled waveguide-fed slot with coaxial input, located at the stagnation point of the reentry nose cone (Figures 6 and 25). The S-band receiving antenna is of identical internal dimensions but with a T-bar feed located at the shoulder of the nose cone (Figure 4) to measure the interantenna mutual coupling. Both antennas were adjusted to provide an impedance match to the input coaxial cable under freespace conditions. The parameters measured on the vehicle include the incident and reflected power for the transmitting antenna and the power coupled to the receiving antenna.

The input admittance and coupling of the plasma-covered slot antenna are difficult to evaluate exactly because the ionized flow fields are nonhomogeneous and the slot is located on a hemispherical metal surface. Fortunately, since the hemisphere is reasonably large—about three wavelengths in diameter—it can be approximated by a ground plane for self-admittance calculations.

The theoretical model that has been evaluated consists of the slot antenna mounted in a flat ground plane of infinite extent and covered with stratified layers of plasma. Two computer programs were made available for analyzing the flight

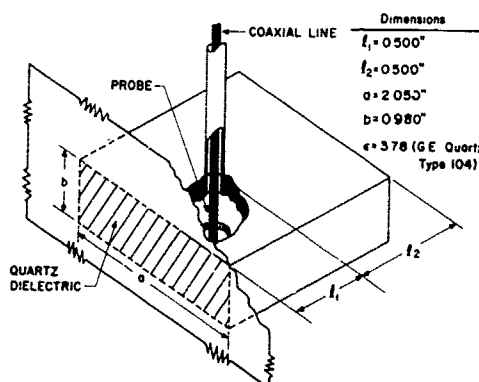


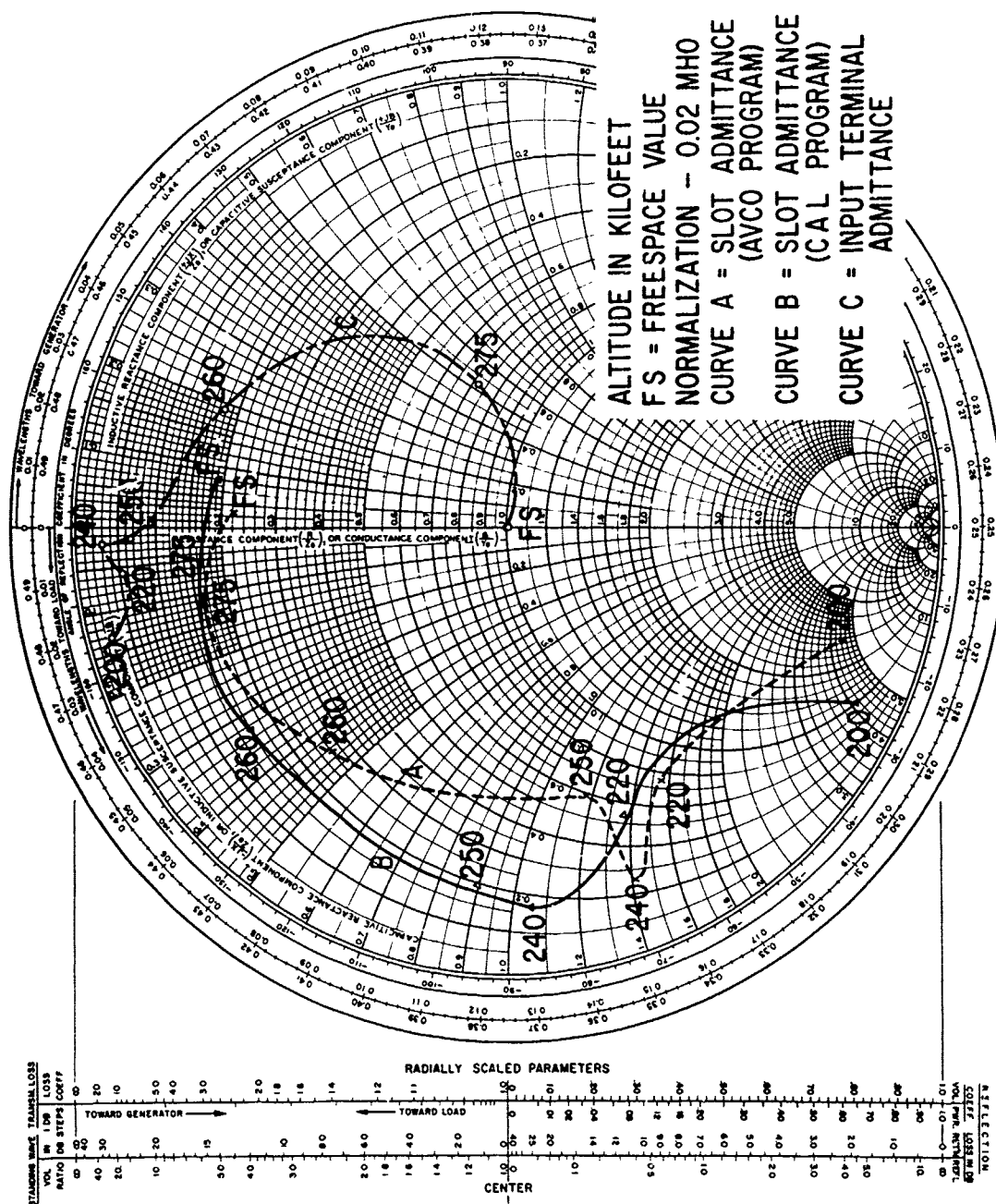
Figure 25. Dimensions of Nose Cone Slot Antenna

data. The first, developed by Cornell Aeronautical Laboratory, is based on the theoretical analyses of Galejs (1965). The inputs to this computer program consist of the physical dimensions of a transmitting antenna and of an identical receiving antenna on the same ground plane, the separation between the two antennas, terminating admittance for the receiving antenna, and the electron density, collision frequency, and thickness of each plasma layer. The output of the program consists of the terminal admittance of the transmitting antenna (normalized to the wave admittance of the waveguide at the slot reference plane) and the mutual admittance and coupling between the two antennas. The second computer program, developed by Fante, McLaughlin, and Trousdale at Avco (1966), gives the far-field radiation patterns, as well as the terminal admittance, for the open-ended waveguide.

The plasma sheath properties used in the calculation of self-admittance and radiation patterns are those that exist at the stagnation point of the nose cone. This assumption neglects the variation of plasma properties over the slot aperture and ground plane and also the displacement of the slot from the stagnation point (the nose cone entered at about a 12° angle of attack). The stagnation region flow field properties are calculated for a range of altitudes from 200 to 275 kft and at a reentry velocity of about 16.5 kft/sec. Nonequilibrium effects are taken into account and the inviscid and boundary layer results are merged to form a single profile for the whole plasma sheath. These calculations are discussed in detail in Sec. 3.5.

The plasma parameters are evaluated at the stagnation point of the vehicle as a function of the normal distance from the body surface. This continuous variation of plasma parameters is then approximated piecewise with 7 to 10 homogeneous slabs, depending on the altitude. The slab closest to the vehicle skin has unit relative permittivity (free space). Tabulated values for some of these flow field calculations, as well as the parameters for the plasma layers used in the computer programs, are given in Appendix A.

The computed terminal admittance for the antenna slot aperture, normalized to the wave admittance of the dielectric-filled waveguide, is plotted as a function of altitude in the Smith Chart reproduced as Figure 26. The three curves in this figure represent the results of (A) the Avco computer program and (B) the Cornell Aeronautical Laboratory program; (C), the input admittance to the slot antenna, will be discussed later. Since the same input data was used for both the Avco and CAL programs, the differences between curves A and B represent discrepancies in the physical models used in formulating the problem. Also, the solutions obtained from the CAL computer program are sensitive to the presence of surface wave singularities and may be subject to error for low-loss overdense plasmas.



Although these two programs have not been subjected to critical comparison, a routine examination discloses their close agreement on plasmas with moderate or high losses, underdense plasmas, or layers of real dielectrics.

The theoretical aperture admittance for the transmitting antenna cannot be compared directly with the flight data measurements of the reflected power at its coaxial input since this admittance is transformed to a different value at the coaxial input by the network comprised of the antenna feed and matching elements.* An equivalent circuit (Figure 27) for the antenna feed network that transforms the external aperture admittance into the input coaxial admittance was therefore derived from the physical dimensions of the slot antenna (Jennetti and Fujimoto, 1965; also, Jennetti, 1965). Since the final adjustments of the antenna feed are experimental, two of the parameters in the circuit (the series reactance X_p and the admittance multiplying factor N , for the ideal transformer) cannot readily be obtained from the physical dimensions. They can, nevertheless, be calculated because the input admittance of the coaxial line to the antenna is matched for free-space conditions and in such case the freespace terminal admittance of the aperture must transform (through the network of Figure 27) to the characteristic admittance of the coaxial line. The derived parameters ($N = 3.72$ and $X_p = 1.114$) complete the characterization of the network so that an arbitrary terminal admittance can be converted to an equivalent input admittance. This procedure was followed in converting the terminal slot admittance obtained from the Avco program (curve A, Figure 26) to the coaxial input admittance to the slot antenna (curve C, Figure 26).

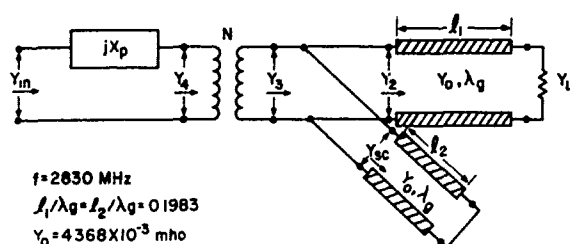


Figure 27. Equivalent Circuit for Slot Antenna

*The OSU experimental and theoretical data (Mayhan et al, 1968; OSU, 1969) can be compared directly for calculations of the slot admittance since the coaxial input to the OSU antenna is matched when the dielectric-filled waveguide is terminated in its characteristic admittance. This makes the input VSWR equal to that at the plane of the slot aperture and the antenna becomes mismatched under freespace conditions. In the present case this freespace mismatch would result in an unacceptably large insertion loss since ground reception of the S-band transmitted signals is necessary for radiation pattern analysis.

Figure 28 compares the theoretical power reflection coefficient R_p for the slot antenna with the measured flight test data. Curve B is the theoretical result with no line loss; curve C is curve B corrected to include a measured attenuation of 1.5 dB in the transmission line between the coaxial input to the antenna and its directional coupler where the reflected power is measured. The relatively abrupt transition from low to high reflection coefficients that the flight test data (curve A) shows at an altitude of about 230 kft should in theory (curve C) occur at the higher altitude of 260 kft. The maximum value of the reflection coefficient is about the same in the two curves, however, and corresponds to almost total reflected power at altitudes below 200 kft.

The prediction of the aerodynamic properties of the plasma sheath from the flight measurements of antenna mismatch will now be considered. The general solution to determine the complete plasma sheath profile, including electron density and collision frequency, requires measurements of the slot admittance over a distinct number of frequencies (Mayhan, 1968), starting with some reasonable estimate of the shape of the plasma sheath. In the present case, however, the pertinent flight data consists of measurements of a single parameter, the reflection coefficient of the slot antenna, as a function of altitude. Fortunately, an extensive study (Croswell et al, 1968) of the admittance of the waveguide-fed aperture under an inhomogeneous plasma shows a clear separation of the dependence of the admittance parameters on plasma properties: for critical and overdense plasmas, the collision frequency primarily affects the aperture conductance whereas the profile shape or boundary layer primarily affects the aperture susceptance. At altitudes above 200 kft, where the collision frequency is small compared with the operating frequency, the plasma can be treated as a lossless medium. The

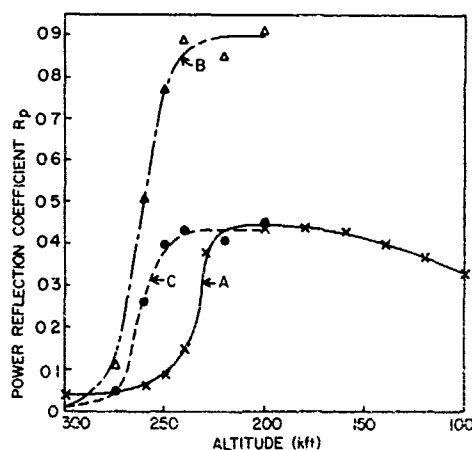


Figure 28. Power Reflection Coefficient Versus Altitude for Nose Cone Slot Antenna [(A) flight test measurements; (B) theoretical PRC, no line loss; (C) theoretical PRC, 1.5-dB line loss]

slot admittance (hence, power reflection coefficient) depends primarily on a single parameter, the electromagnetic boundary layer thickness δ , which is here defined as the normal distance from the surface of the nose cone to the point in the plasma sheath where the electron density reaches the critical value for the operating frequency. The electromagnetic boundary layer is thus observed to be a function of frequency as well as of the plasma parameters. That the aperture conductance is relatively independent of changes in electron density profile can be observed in the theoretical admittance curves A and B of Figure 26, where the susceptance varies much more rapidly than the conductance as a function of altitude and increasing electron density. [This same type of behavior is evident in the OSU (1969) flight test data, under somewhat different operating conditions.] The power reflection coefficient should therefore be a unique indicator of the thickness of the electromagnetic boundary layer.

The theoretical electromagnetic boundary layer thickness δ , obtained from Table A2 in Appendix A, is shown as the solid line in Figure 29. This data and the admittance-versus-altitude characteristics of curve C in Figure 26 convert to an approximately linear relationship between the power reflection coefficient and the electromagnetic boundary layer thickness (Figure 30). The measured power reflection coefficient obtained from the flight data (curve A of Figure 28) and corrected for the 1.5-dB line loss then gives the experimentally determined boundary layer thickness δ (broken line in Figure 29). The two curves in Figure 29 indicate that the theoretical and derived electromagnetic boundary layer thicknesses both decrease with altitude at about the same rate. They are displaced from each other by about 20 kft in altitude, however, and this discrepancy has yet to be explained. In an attempt to discover its cause, more refined flow field calculations than the merged flow solutions used in this report are being programmed to obtain corrections in the plasma layer data. The difference in boundary layer thickness between theoretical solution and flight data at altitudes below 220 kft is not considered significant because transmission line attenuation prevents accurate measurement of the large reflection coefficients obtained with small boundary layers.

Mutual coupling, defined as the ratio of the power received at the slot antenna on the shoulder of the nose cone to the transmitter power incident on the waveguide-fed slot antenna at the stagnation point, is shown in Figure 31 as a function of altitude, normalized to the freespace value. The flight data for this coupling shows, first, a small increase over the freespace value, starting at 300 kft, and then an abrupt decrease of greater than 10 dB at about 250 kft. At levels lower than -11 dB the coupling was below the dynamic range of the instrumentation and could therefore not be measured at altitudes below 240 kft. The initial increase in coupling may be caused by 'trapped' waves propagating principally in the low plasma density region

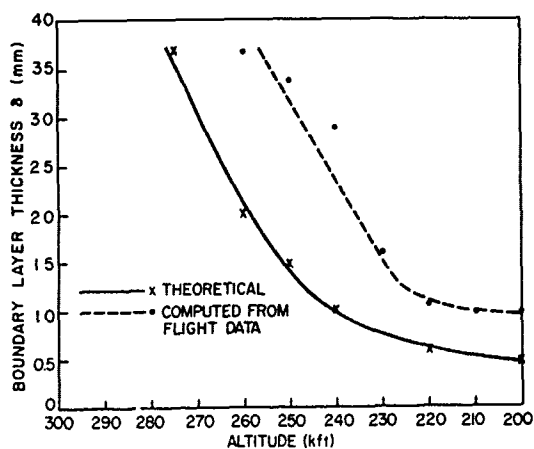


Figure 29. Electromagnetic Boundary Layer Thickness δ Versus Altitude

Figure 30. Power Reflection Coefficient Versus Boundary Layer Thickness for Slot Antenna

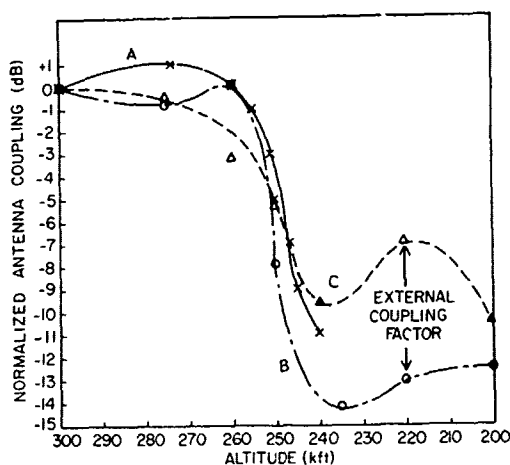
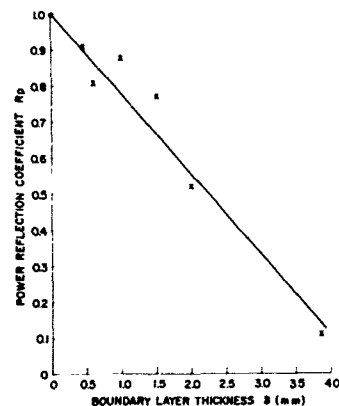


Figure 31. Mutual Coupling Loss Versus Altitude for Two Slot Antennas on Nose Cone [(A) flight test measurements; (B) theoretical antenna coupling; (C) power reflection loss in transmitting antenna]

between the ground plane and the emerged boundary layer—shock interface. The abrupt decrease in coupling at the 250-kft altitude level is apparently caused by the increase in reflected power at the transmitting antenna rather than by any external coupling losses, as evidenced by the following analysis.

Estimation of the mutual coupling between the two antennas on the nose cone is complicated by several factors not included in the computer model of two slots in an infinite ground plane covered by homogeneous plasma layers. First, because of the curvature of the hemispherical nose cone, the value measured for freespace coupling (no plasma layers) is considerably smaller than the value computed for the two slots on a ground plane (-38 dB versus -32 dB). Second, each layer in the physical plasma sheath varies in electrical properties such as electron density by as much as two orders of magnitude in the region between the two slots, whereas the computer program assumes homogeneous layers. The mathematical computations must therefore be considered as only a qualitative estimate of the mutual coupling since more rigorous calculations, including curved surfaces and non-homogeneous plasma layers, are beyond the scope of the present program.

The input data to the CAL computer program for mutual coupling requires the value of the terminating admittance of the receiving antenna, as well as physical dimensions and electrical properties of the plasma layers. This terminating admittance is not equal to the characteristic admittance of either the waveguide feeding the slot or of the coaxial line feeding the antenna but can instead be shown to be the complex conjugate of the terminal (external) admittance of the slot antenna under freespace conditions (Montgomery et al, 1948), as follows.

Assume that the slot antenna is represented by a lossless network (see Figure 32) driven by a constant current source I that matches the terminal admittance of the slot Y_L to the characteristic admittance of the coaxial input $Y_g (=G)$. For maximum power transfer the admittance looking toward the load must at any point in the network be the conjugate image of the admittance looking toward the source. ['any point' includes both the input and output terminals.] The admittance of the network at reference plane No. 1 is:

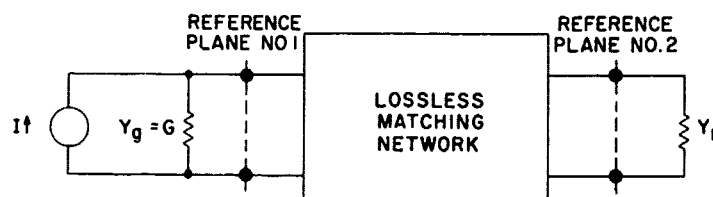


Figure 32. Network Diagram for Conjugate Admittance Theorem

$$Y_{in_1} = G, \quad (12)$$

which meets the condition for a matched coaxial input. At reference plane No. 2, the admittance looking toward the source is

$$G_{in_2} = G_L; B_{in_2} = -B_L, \quad (13)$$

or,

$$Y_{in_2} = Y_L^*. \quad (14)$$

Thus, the load admittance, which represents the receiving antenna in the mutual admittance calculations, is equal to the conjugate of the freespace terminal admittance of the antenna slot aperture when the coaxial input is matched under free-space conditions.

The mutual coupling is defined as the ratio P_{coup}/P_{inc} , where P_{inc} is the incident power at the coaxial input to the transmitting antenna, and P_{coup} is the received power in the load of the receiving antenna. It can be conveniently separated into two factors:

$$P_{coup}/P_{inc} = \left(\frac{P_{rad}}{P_{inc}} \right) \left(\frac{P_{coup}}{P_{rad}} \right), \quad (15)$$

where P_{rad} is the power radiated from the slot aperture of the transmitting antenna. The first factor in Eq. (15) is simply related to the power reflection coefficient R_p for the transmitting antenna, as

$$P_{rad}/P_{inc} = 1 - R_p. \quad (16)$$

This factor (P_{rad}/P_{inc}) is obtained from curve B of Figure 28 and replotted as the theoretical power reflection loss curve of Figure 31.

The second factor (P_{coup}/P_{rad}), the 'external coupling factor,' is the ratio of received-to-transmitted power for the two antennas. It is arbitrarily taken as one-third of the external mutual coupling factor for the two antennas, with the homogeneous plasma layers corresponding to the stagnation point values, and it is corrected for the freespace coupling. The factor of one-third is selected pragmatically since only about one-third of the distance between the two antennas is

covered with an overdense plasma at these altitudes. This external coupling factor, shown as the difference between the power reflection loss and the theoretical antenna coupling curves in Figure 31, may be greater or smaller than unity, depending on altitude. Considering the crude nature of these approximations, the theoretical and flight test measurements of antenna coupling compare reasonably well, both curves showing a very sharp decrease in coupling at an altitude of about 250 kft.

5.2 Signal Attenuation and Radiation Patterns

The radiation pattern of a slot in the hemisphere cone reentry vehicle is rather difficult to determine analytically. If, however, the radius of curvature of the metal surface in which the slot is mounted is on the order of a wavelength or larger, the radiation characteristics at angles within the forward hemisphere and within about 60° from the longitudinal axis of the nose cone should be similar to those of the slot in an infinite ground plane (Cohn and Morita, 1955). Since the hemisphere is about 1.5λ in radius at the S-band transmitter frequency, this replacement of the complex missile body by a flat ground plane is a reasonable approximation, subject to further verification as described in the following paragraphs.

The intensity of the signal received at the ground antenna depends on the field strength at the receiving site and the relative polarization of the transmitter and receiver. The radiation pattern can therefore be expressed as the product of an amplitude factor and a polarization factor. The model, a slot in an infinite ground plane, is assumed to have a uniform electric field variation in the narrow dimension of the aperture and a cosinusoidal variation in its wide dimension; the corresponding amplitude factor, $g(\theta, \phi)$, of the radiation pattern is given (Silver, 1949) by:

$$g(\theta, \phi) = \left[\frac{\sin\left(\frac{\pi b}{\lambda} \sin \theta \sin \phi\right)}{\left(\frac{\pi b}{\lambda} \sin \theta \sin \phi\right)} \right] \left[\frac{\cos\left(\frac{\pi a}{\lambda} \sin \theta \cos \phi\right)}{1 - \frac{4}{\pi^2} (\sin \theta \cos \phi)^2} \right]. \quad (17)$$

Here, λ is the freespace wavelength. The other parameters are defined in Figure 33, where θ and ϕ are respectively the polar and roll angles relative to the longitudinal axis of the nose cone. The corresponding polarization factor $p(\theta, \phi)$, derived in Appendix B, is given by

$$p(\theta, \phi) = \frac{\sin \phi}{(1 - \sin^2 \theta [1 - \sin^2 \phi])^{1/2}}. \quad (18)$$

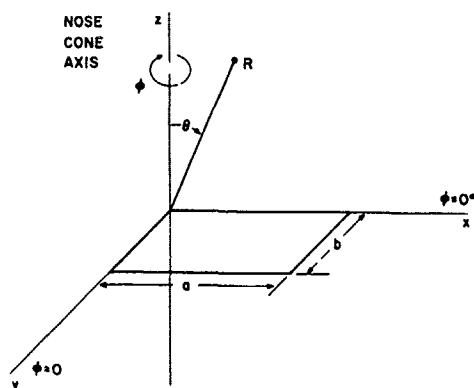


Figure 33. Coordinate System for Radiation Patterns of Slot Antenna

Equations (17) and (18) are used to compute the relative changes in signal strength at the ground receiving site as a function of time during reentry for altitudes of 300 to 200 kft, corresponding to freespace to blackout conditions respectively. The polar angle θ is taken as a constant value of 45° in these calculations since it changes by no more than 5° over this range of altitudes (Sec. 3.4). The roll rate of the nose cone and the range to the ground site do not change significantly and are also considered to be constant. The theoretical amplitude factor $g(\theta, \phi)$, polarization factor $p(\theta, \phi)$, and composite radiation pattern $[g(\theta, \phi) \cdot p(\theta, \phi)]$ versus roll angle are shown in Figure 34. The sharp nulls caused by cross polarization of the nose cone slot and the ground antenna at $\phi = \pm 90^\circ$ are evident. In Figure 35, this composite radiation pattern is compared with the radiation pattern of the slot on a model of the Trailblazer II nose cone (measured on an antenna test range) and with an inflight pattern derived from the received signal at the ground terminal (measured at a reentry altitude of 295 kft, at which plasma sheath effects are negligible). The comparison shows, first, that the pattern of the slot antenna on a flat ground plane is a good approximation to that of the slot antenna on the nose cone measured in the forward region and, second, that laboratory radiation pattern measurements can accurately reproduce inflight measurements at the receiver site.

The signal strength at the ground receiver site is shown in Figure 36 as a function of decreasing altitude. The flight data curve is the peak value of signal strength observed during each rotation of the nose cone, and corresponds to the nose cone orientation ($\phi = 90^\circ$) for which the transmitting and receiving antennas are colinearly polarized. The theoretical curve is derived from the same flow field and plasma parameters used (Sec. 5.1) to evaluate the terminal and input admittances of the cavity-slot antenna, based on the Avco computer program for the radiation pattern calculations.

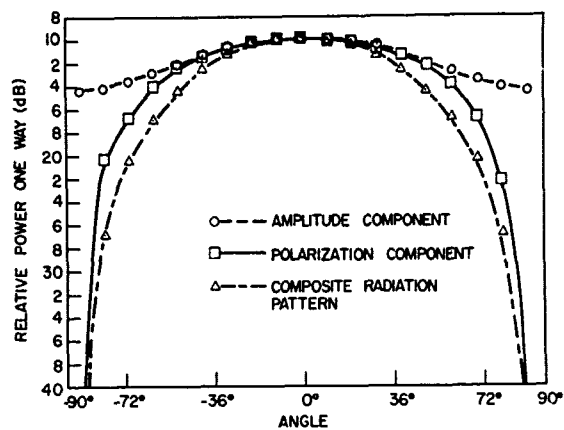


Figure 34. Theoretical Radiation Pattern of Slot in Ground Plane

Figure 35. Freespace Radiation Patterns for Trailblazer II Nose Cone Antenna

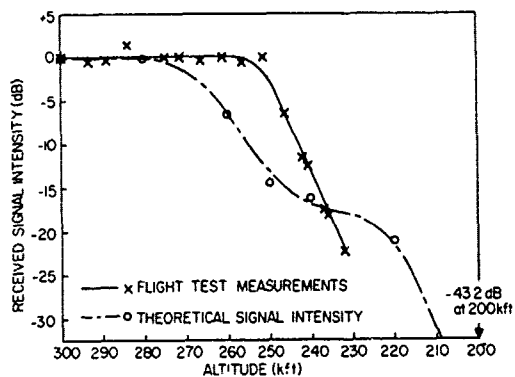
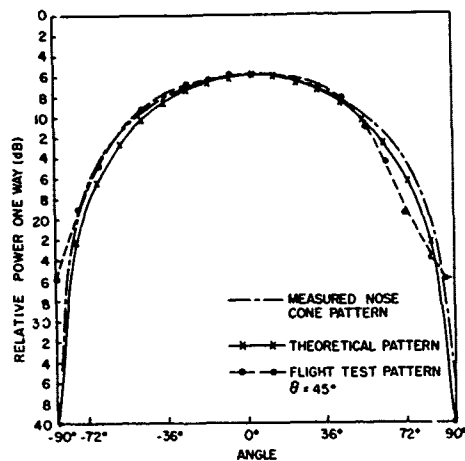


Figure 36. Received Signal Intensity Versus Altitude for Slot Antenna on Nose Cone

The calculations of the antenna radiation patterns were corrected for the difference between the power reflection coefficient as measured at the coaxial input to the slot antenna and as computed for the reflected power in the waveguide feeding the slot aperture. The Avco program computed the insertion loss and signal attenuation through the plasma sheath on the basis of a constant level of incident power in the waveguide, whereas the flight test measured the signal attenuation with constant incident power in the coaxial line. The received power at the ground station, P_{rec} , is related to the computed value from the Avco program $(P_{\text{rec}})_{\text{Avco}}$ by the factor:

$$P_{\text{rec}} / (P_{\text{rec}})_{\text{Avco}} = 1 / (1 - R_p)_{\text{slot}} / (1 - R_p)_g, \quad (19)$$

where $(R_p)_{\text{slot}}$ is the power reflection coefficient at the coaxial input to the slot antenna (Figure 28) and $(R_p)_g$ is the power reflection coefficient in the waveguide feeding the slot aperture, as determined from the computed terminal admittance of the slot.

Comparison of the predicted signal intensity at the ground station with the flight results (Figure 36) indicates that the measured signal intensity falls off less rapidly with decreasing altitude than that theoretically predicted. The flight test data shows almost no change in signal intensity until an altitude of about 250 kft is reached, at which point there is a rapid decrease. The signal attenuation reaches over -20 dB at 230 kft, below which the signal is too weak to be measured. The predicted signal strength, on the other hand, starts decreasing at about 270 kft and reaches the same value as the flight data at about 240 kft. The differences between the predicted and measured signal intensity can to a large extent be accounted for by attenuation due to reflected power losses in the slot antenna, which become significant at an altitude of about 20 kft lower than the predicted value (Figures 28 and 31). The results indicate that the approximate flow field calculations apparently overestimate the electron density at the higher altitudes but are in substantial agreement with flight results at altitudes below 240 kft.

The inflight radiation patterns in Figure 37 show several altitudes at which the signal attenuation is changing substantially. The curves, normalized so that the peak values correspond to zero dB, show that the shape of the radiation pattern does not change substantially even under conditions when the plasma sheath attenuates the signal by over 20 dB. This result has been predicted (Fante, 1967; Fante, Hayes, and Shane, 1967; Aerospace Corp., 1967) for overdense plasma sheaths that are physically thin compared with the wavelength of the transmitted signal. Under these conditions the plasma sheath is equivalent to an impedance

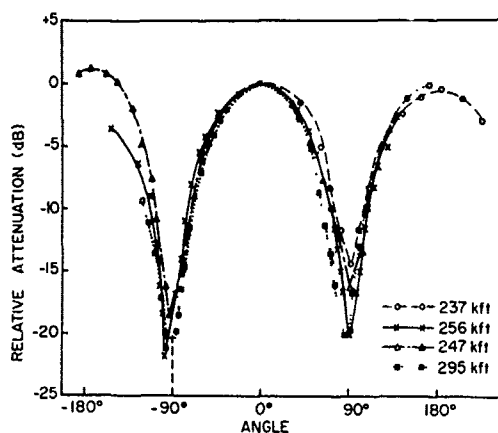


Figure 37. Radiation Patterns Versus Altitude:
Trailblazer II Flight Data

sheet that attenuates the signal level without changing the pattern shape. This conclusion has also been confirmed by the Avco computer calculations, which show that the radiation patterns are attenuated, but otherwise unchanged in shape, as a function of altitude.

6. DISCUSSION

Comparison of the probe measurements of Sec. 4 with the flow field calculations of Sec. 3 shows an apparent discrepancy. The flow field curves of Figure 18 indicate that at an altitude of 240 kft, an electron density of $2 \times 10^{10} \text{ el/cm}^3$ is reached at a distance of about 0.5 mm from the surface at the stagnation point of the nose cone. Since the electron density along the outer edge of the boundary layer decreases with distance back along the vehicle from the stagnation point (Figure 17), it would be reasonable to suppose that before the electron density in the boundary layer would reach an equivalent value at the shoulder, the distance from the vehicular surface to a point on the plasma sheath profile would have to be considerably greater than the 0.5-mm value. On the contrary, the EA probe No. 1 located at the shoulder measured this distance as 0.1 mm [Figure 24(a): $m = 1$ curve], about one-tenth that predicted by the flow field calculations (Sec. 3).

In contrast to this situation, the microwave measurements do not show extreme disagreement with the flow field predictions. The electromagnetic boundary layer thickness δ (Sec. 5.1) is postulated as a measure of the distance from the vehicular surface to the point in the plasma sheath where the plasma becomes overdense

($n_e \approx 10^{11}$ el/cm³ at S-band frequencies). At 240 kft, δ measures about 2 mm (Figure 29) at the stagnation point, about twice the value predicted from flow field calculations (Figure 16). The microwave measurements therefore compare with the flow field calculations five times better than the electroacoustic probe data.

More exact predictions (Bredfeldt et al, 1967; Ball et al, 1965), of the flow fields, including nonequilibrium effects in the boundary layer that were neglected in this report, indicate that the electron density gradient near the vehicular surface is much greater than appears in the profiles of our Figure 16. These other workers predict that after an initial sharp rise in electron density, the plasma sheath profile is relatively flat in the vicinity of the maximum electron density. This type of profile could account for the apparent discrepancy between the measurements obtained with the EA probe and the microwave antenna, and is being calculated for the Trailblazer II nose cone.

An additional factor to be considered is the dependence of the electromagnetic boundary layer thickness δ on the shape of the electron density profile since estimation of this boundary layer thickness for Figure 29 was based on a particular set of shapes for the profiles whereas the actual shapes are in doubt. The voltage reflection coefficient $|\rho|$ of the S-band slot antenna was therefore calculated for six different electron density profiles in which the position of the critically dense layer was kept constant while the electron density distribution in the underdense region between this layer and the vehicular surface was drastically changed. The profile selected as the standard for comparison was that given in Figure 16 for an altitude of 240 kft. The results (Appendix A) indicate that the magnitude of the reflection coefficient is insensitive to changes in the electron density distribution in the underdense region and for a given antenna geometry depends principally on the position of the critically dense region. The electromagnetic boundary layer thickness δ , as derived from measurements of reflected power from the antenna, is therefore a valid estimate of the position of the critically dense plasma layer in thin plasma sheaths.

7. CONCLUSIONS

Flow field calculations of electron density that assume separate boundary and shock layers do not give results that agree with observations for altitudes between 200 and 300 kft. Much better agreement is obtained with the merged flow solutions. In addition, calculation of electron density gradients near vehicular surfaces require consideration of nonequilibrium effects in the boundary layer. This conclusion is substantiated by nonequilibrium computations (Ball et al, 1965) whose results for the theoretical electron densities near the vehicular surfaces are substantially

different from those obtained in the flow field analyses of Sec. 3 (Figure 16), and by the electrostatic probe measurements. The electron densities inferred from the probe measurements agreed, however, with the calculated equilibrium values from 100 to 230 kft within a factor of less than 3.

The precession and roll angle of the nose cone can be readily observed from the cyclic variation in the output of the electrostatic and electroacoustic probes. The initial angle of attack was predictable from trajectory data and the assumption that the rocket thrust of the fourth stage was aligned with the body axis of the nose cone.

The temporal development of the plasma sheath to the point where it affects the performance of the microwave antennas apparently occurs at an altitude about 20 kft lower than that predicted by theory. This discrepancy, which is simultaneously observed in the measurements of the antenna admittance and coupling, and in the attenuation of the signals received at the ground stations, has not yet been satisfactorily explained.

Power reflection measurements on the S-band slot antenna give considerable information on the structure of the plasma sheath immediately over the surface of the aperture. The admittance of a slot antenna covered by a thin overdense plasma depends primarily on antenna geometry and distance to the critically dense plasma layer. The power reflection coefficient of the antenna, which is uniquely related to its admittance, therefore gives an estimate of this critical distance.

Attenuation of the S band signal in the vehicle-to-ground transmission link is due almost entirely to reflective, rather than resistive, losses from the plasma in front of the nose cap antenna. The shape of the radiation pattern does not change, even when the plasma is attenuating the signal by over -20 dB. This invariance of pattern shape is predictable from computer analysis of antennas covered by thin overdense plasmas.

The variation in coupling between the nose cap and shoulder antennas is caused principally by reflected power losses in the transmitting antenna. The external coupling factor cannot be calculated with any degree of accuracy because the plasma layers are not uniformly stratified and the antennas are on a curved surface. The small increase in coupling (about 1 dB) at altitudes between 300 and 270 kft may possibly be caused by surface waves or trapped waves within the plasma.

The plasma diagnostic system of four electroacoustic probes and three flush-mounted electrostatic probes proved very helpful in evaluating the profile of the plasma sheath. The measurements obtained with both types of probes agreed substantially. The successful operation of the EA probes showed, for the first time, that electroacoustic waves may be used as a diagnostic means for inflight reentry plasma sheath measurements. This application is probably restricted to

altitudes above 200 kft since the high collision frequencies at lower altitudes tend to eliminate the resonances.

A second Trailblazer II vehicle in this flight series was successfully launched from Wallops Island, Va., in June 1969. The payload was similar in many respects to that described in this report. New data from this flight included high-power microwave interactions with the plasma sheath, changes in the radiation pattern shape of the S-band telemetry antennas, and greatly improved resolution of the probe and microwave antenna measurements. These results will appear in an AFCRL Technical Report soon to be published.

Rocket flights planned for the near future will investigate the nature of the plasma sheath in the expansion region of the flow fields, the effects of chemical additives in reducing electron density, and some other plasma diagnostic techniques. These studies are expected to lead to a closer understanding of the nature of the plasma sheath and the results applied to achieve improvements in reentry communication systems.

Acknowledgments

The authors wish to acknowledge the contributions of many individuals and organizations to the success of this Trailblazer II rocket flight. Personnel in charge of the design, test, and fabrication of the nose cone and its scientific payload include L. Poirier (coauthor) as AFCRL project scientist; R. Walters, AFCRL, in Mechanical Design; and R. Sukys, Northeastern University, in Electronic Systems. The electroacoustic probes were designed by C. Lustig of Sperry Rand, and the electrostatic probes by J. Chown of Stanford Research Institute. Electronic subsystems and antennas were designed and constructed by D. Tropea, N. Karas, and J. Antonucci, all of AFCRL. Launch support was provided by the personnel of the NASA Wallops Island, Va., Rocket Launch Facility, with D. Bruton as the project engineer. Special ground receiving sites for telemetry and signal attenuation measurements were made available through the AFCRL experimental radars at Wallops Island under the direction of J. Howard of Johns Hopkins University. Captain W. Weppner, formerly of AFCRL and now at the NASA Manned Flight Center, served as project coordinator for range support. The two computer programs for plasma-covered antennas were made available for this project by E. Shane of Avco, and R. Tripp of Cornell Aeronautical Laboratory.

References

- Aerospace Corporation (1966) Lifting Reentry Communications: Vol. I, A comparative evaluation of potential systems, Rpt No. TR-669(6220-10)-3 (I) [AFSC Contracts No. AF04(695)-669 and AF04(695)-1001; Rpt No. SSD-TR-66-73 (I)], May 1966.
- Aerospace Corporation (1967) Lifting Reentry Communications: Vol. III, Plane wave attenuation tables, Rpt No. TR-669(6220-10)-3 (III) [AFSC Contracts No. AF04(695)-669 and AF04(695)-1001; Rpt No. SSD-TR-66-73 (III)], February 1967.
- Bachynski, M. P. (1967) Sources in plasmas, RCA Review 28:111-152, March 1967.
- Baldwin, K. M., Basset, O. E., Hawthorne, E. I., and Langberg, E. (1961) Telecommunications during reentry, in Electromagnetic Effects of Reentry, W. Rotman and G. Meltz, Eds., Pergamon Press, pp. 207-218.
- Ball, W. H., Webb, H. G., Jr., and Lyon, F. J. (1965) Flow Field Predictions and Analysis Study for Project RAM B3, Space and Information Systems Division Final Rpt No. SID-65-1113, Rpt No. NASA-CR-66106 [Contract NAS 1-4743], North American Aviation, Inc., 20 August 1965.
- Bohm, D., Burhop, E. H. S., and Massey, H. S. W. (1949) The use of probes for plasma exploration in strong magnetic fields, in The Characteristics of Electrical Discharge in Magnetic Fields, A. Guthrie and R. K. Wakerling, Eds., McGraw-Hill, pp. 13-76.
- Bredfeldt, H. R., Scharfman, W. E., Guthart, H., Morita, T. (1967) Boundary-layer ion density profiles as measured by electrostatic probes, AIAA J. 5 (No. 1):91-98, January 1967.
- Caldecott, R., Bohley, P., and Nerem, R. (1967) Reentry Communications: Antenna Impedance and Radar Reflection Recorded During the Reentry of a Trailblazer Rocket Vehicle on 14 February 1966, Electrosience Laboratory Rpt No. 2146-7 [Contract AF33(615)-3466], Ohio State University Research Foundation, January 1967.

- Chen, F. F. (1965) Electric probes, Chap. 4 in Plasma Diagnostic Technique, R. H. Huddleston and S. L. Leonard, Eds., Academic Press, New York.
- Chung, P. M., and Blankenship, V. D. (1966) Theory of Electrostatic Double Probe Comprised of Two Parallel Plates, Rpt No. TDR-469(S5240-10)-3, [Contract No. AF04(695)-469], Aerospace Corporation, April 1965, corrected March 1966.
- Cohn, S. B., and Morita, T. (1955) Microwave Radiation From Large Finite Bodies, Rpt No. 48 [AFCRL Contract AF19(604)-1296], Stanford Research Institute, January 1955.
- Croswell, W. F., Taylor, W. C., Swift, C. T., and Cockrell, C. R. (1968) The input admittance of a rectangular waveguide-fed aperture under an inhomogeneous plasma: theory and experiment, IEEE Tr. AP, AP-16:475-487, July 1968.
- Curtis, J., Burke, A., and Hayman, R. (1963) An Analytical and Experimental Study of the Ionized Flow Field About a Hemisphere Cylinder and Its Effect on the Radiation Pattern of a Slot Antenna, Final Rpt No. AFCRL-63-339 [Contract AF19(604)-8494], Cornell Aeronautical Laboratory, August 1963.
- Evans, J. S., and Huber, P. W. (1963) Calculated Radio Attenuation Due to Plasma Sheath on Hypersonic Blunt-nosed Cone, NASA Tech. Note No. TDN-2043, December 1963.
- Ewald, H. N. (1968) Electroacoustic Resonances in a Nonuniform Plasma, Sci. Rpt No. 1 [Contract No. F19628-67-C-0096], Sperry Rand Research Center, Sudbury, Mass., October 1968.
- Fante, R. L. (1967) Effect of thin plasmas on an aperture antenna in an infinite ground plane, Radio Science 2(NS)(No. 1):87-100, January 1967.
- Fante, R. L., Hayes, J. J., and Shane, E. D. (1967) Systems approach to the reentry communications problem, Vol. I, Proc. Conf. Applications of Plasma Studies to Reentry Vehicle Communications, 3-4 October 1967, sponsored by Air Force Avionics Laboratory (AVWE-3), Wright-Patterson AFB in conjunction with Ohio State University.
- Fante, R. L., McLaughlin, J. R., and Trousdale, J. E. (1966) A Study of Ablation Material Effects on Antenna Performance, Rpt No. AVSSD-0277-66-RR [NASA Contract 9-4916], Sec. C, Avco Corporation, Wilmington, Mass.
- Galejs, J. (1965) Self and mutual admittances of waveguides radiating into plasma layer, Radio Science (J. Res. NBS) 69D:179-189, February, 1965.
- Hartsel, J. E., and Nerem, R. M. (1964) Predicted Reentry Performance of a Trailblazer II Vehicle, Rpt No. 1573-7 [Contract AF33(650)-10523], Ohio State University, September 1964.
- Jennetti, A. G., and Fujimoto, K. (1965) Design Considerations for a Slot Antennifier, Rpt No. 1566-20, Wright-Patterson AFB, Contract AF33(657)-10386, Ohio State University, 25 September 1965. See also, Jennetti, A. G. (1965) A 1-Gc Cavity-Back Slot Antennifier, Rpt No. 1566-23 [Wright-Patterson AFB, Contract AF33(657)-10386], Ohio State University, 22 November 1965.
- Lustig, C. D., and McBee, W. D. (1969) Proposed Method of Measurement of Electron Density in Reentry Sheaths by Observation of Electroacoustic Resonances, AFCRL-69-0039 (AD686458), Sci. Rpt No. 2 [Contract No. F19628-67-C-0096], Sperry Rand Research Center, Sudbury, Mass., February 1969.

- Mayhan, J.W. (1968) Plasma Diagnostics Using the Reflection Coefficient of Planar Antennas, Electrosience Laboratory Rpt No. 2146-11 [Wright-Patterson AFB, Ohio, Contract AF33(615)-3466], Ohio State University, 25 October 1968.
- Mayhan, J.W., Caldecott, R., and Bohley, P. (1968), Antenna impedance in a reentry environment, IEEE Tr. AP, AP-16:573-577, September 1968.
- Montgomery, C.G., Dicke, R.H., and Purcell, E.M., Eds. (1948) Principles of Microwave Circuits [MIT Rad. Lab. Ser. Vol. 8], McGraw-Hill, Sec. 4,3, p. 95.
- Nerem, R. (1962) Stagnation Region Plasma Properties Including Some Nonuniform Effects, Aerodynamics Laboratory Rpt No. 1021-25 [Contract No. AF33(616)-6782], Ohio State University Research Foundation, December 1962.
- Ohio State University (1969) Ion Sheath Propagation Studies, Electrosience Laboratory Rpt. No. 2146-13, Tech. Rpt No. AFAL-TR-69-53 [Wright-Patterson AFB, Ohio, Contract No. AF33(615)-3466], Ohio State University, 6 May 1969.
- Proc. Conf. Applications of Plasma Studies to Reentry Vehicle Communications, 3-4 October 1967 (Vol. I), sponsored by Air Force Avionics Laboratory (AVWE-3), Wright-Patterson AFB in conjunction with Ohio State University.
- Rotman, W., Moore, H.K., and Papa, R., Eds. (1964) Electromagnetic Aspects of Hypersonic Flight, Spartan Books, Inc., Baltimore, Md. [Unclassified papers presented at Proc. Second Symposium on the Plasma Sheath: Its Effect Upon Reentry Communication and Detection, held at Boston, Mass., 10-12 April 1962.]
- Rotman, W., Moore, H., Papa, R., and Lennon, J., Eds. (1967) Proc. Third Symposium on the Plasma Sheath: Plasma Electromagnetics of Hypersonic Flight, held at Boston, Mass., 21-23 September 1965, Rpts Nos. AFCRL-67-0280(I)(II)(III), May 1967. [This symposium record consists of three unclassified volumes as follows: (I) Radiation Characteristics of Plasma-Covered Antennas, (II) Electrical Properties of Shock-Ionized Flow Fields, (III) Reentry Plasmas: Simulation, Diagnostics, and Alleviation Techniques. An additional (Secret) volume, covering the classified papers presented at the symposium, is available as Rpt No. AFCRL-66-608, August 1966.]
- Scharfman, W.E., and Bredfeldt, H.R. (1967) Experimental Studies of Electrostatic Probes for the Reentry Measurements Program, Phase B [Final Rpt on Subcontract No. 601603 under Contract DA 30-069-AMC-333Y], Stanford Research Institute, Menlo Park, Calif., July 1967.
- Schmitt, H.J. (1964) Plasma resonances excited by antennas, Proc. IEEE (correspondence) 52:622.
- Silver, S. (1949) Microwave Antenna Theory and Design [MIT Rad. Lab. Ser. Vol. 12], McGraw-Hill, 1949, Table 6.1, p. 187.

Appendix A

Plasma Sheath Data for Slot Antenna Calculations

This section presents the numerical input data used in the CAL and Avco computer programs to calculate the terminal admittance, isolation, and radiation patterns of the plasma-covered slot antenna (Secs. 5 and 6). Standard floating point, as well as fixed point, notation is used, the number being represented by a real constant between 0.1 and 1.0, followed by the letter E and an integer power of 10 by which the number is to be multiplied. The slot parameters (Figure 25) used in all calculations are:

Frequency	2.830 GHz
Slot Width (a)	5.182 cm
Slot Height (b)	2.489 cm
Slot Separation (E plane)	29.101 cm
Dielectric constant of quartz in waveguide	3.780

The idealized antenna model, used in the computer calculations, includes a number of homogeneous plasma layers above the antenna. The parameters for these layers at the stagnation point of the nose cone are derived from a quantization of the electron density in Figure 16 and estimates of collision frequencies from Figure 17. The electrical properties of each layer (slab) are specified (Table A1) by the width of the slab, electron density, and collision frequency, starting with the outer edge of the shock layer and ending with a layer next to the ground plane of zero electron density. Seven to ten plasma layers describe each

Table A1. Electrical Properties of Plasma Layers at Stagnation Point of Nose Cone

Altitude (kft)	Slab No.	Slab Width (cm)	Electron Density (e1/m ³)	Collision Frequency (sec ⁻¹)	Dielectric Constant	
					Real	Imag.
200	1	0.050	0.15E 17	0.70E 11	0.990	0.035
	2	0.100	0.90E 17	0.70E 11	0.945	0.215
	3	0.350	0.20E 19	0.70E 10	-16.408	6.853
	4	0.140	0.13E 20	0.70E 10	-112.155	44.546
	5	0.040	0.17E 20	0.70E 10	-146.972	58.252
	6	0.160	0.13E 20	0.70E 10	-112.155	44.546
	7	0.025	0.10E 19	0.35E 10	-8.678	1.905
	8	0.025	0.10E 17	0.18E 10	0.900	0.010
	9	0.006	0.10E 15	0.75E 09	0.998	0.000
	10	0.003	0.	0.	0.999	0.
220	1	0.050	0.16E 16	0.60E 11	0.998	0.004
	2	0.200	0.20E 17	0.60E 11	0.983	0.054
	3	0.200	0.35E 18	0.30E 10	-2.421	0.577
	4	0.270	0.32E 19	0.30E 10	-30.280	5.277
	5	0.060	0.51E 19	0.30E 10	-48.852	8.410
	6	0.060	0.18E 19	0.30E 10	-16.595	2.968
	7	0.015	0.10E 18	0.15E 10	0.001	0.084
	8	0.015	0.10E 17	0.10E 10	0.899	0.005
	9	0.010	0.10E 16	0.50E 09	0.989	0.000
	10	0.020	0.	0.	0.999	0.
240	1	0.075	0.15E 16	0.10E 11	0.988	0.006
	2	0.050	0.56E 16	0.10E 11	0.975	0.024
	3	0.075	0.20E 17	0.10E 11	0.847	0.085
	4	0.100	0.30E 18	0.10E 11	-1.291	1.288
	5	0.300	0.22E 19	0.15E 10	-20.950	1.852
	6	0.075	0.20E 18	0.15E 10	-0.996	0.168
	7	0.050	0.10E 16	0.50E 09	0.989	0.000
	8	0.025	0.	0.	0.999	0.
250	1	0.020	0.10E 16	0.10E 11	0.992	0.004
	2	0.045	0.44E 16	0.10E 11	0.966	0.018
	3	0.075	0.76E 17	0.10E 11	0.419	0.326
	4	0.100	0.76E 18	0.80E 09	-6.625	0.343
	5	0.200	0.16E 19	0.80E 09	-15.052	0.722
	6	0.100	0.76E 18	0.80E 09	-6.625	0.343
	7	0.070	0.32E 17	0.10E 09	0.678	0.001
	8	0.020	0.10E 16	0.10E 09	0.989	0.000
	9	0.020	0.	0.	0.999	0.
260	1	0.025	0.10E 16	0.10E 11	0.992	0.004
	2	0.060	0.10E 17	0.10E 11	0.923	0.042
	3	0.100	0.38E 18	0.60E 09	-2.815	0.128
	4	0.200	0.74E 18	0.60E 09	-6.430	0.250
	5	0.100	0.22E 18	0.60E 09	-1.209	0.074
	6	0.060	0.35E 16	0.10E 09	0.964	0.000
	7	0.020	0.10E 16	0.10E 09	0.989	0.000
	8	0.070	0.	0.	0.999	0.
275	1	0.010	0.10E 16	0.10E 11	0.992	0.004
	2	0.030	0.18E 17	0.10E 11	0.862	0.077
	3	0.275	0.22E 18	0.10E 09	-1.211	0.012
	4	0.100	0.89E 17	0.10E 09	0.105	0.005
	5	0.100	0.70E 16	0.50E 08	0.929	0.000
	6	0.035	0.10E 16	0.50E 08	0.989	0.000
	7	0.115	0.	0.	0.999	0.

altitude, depending on the shape of its electron density profile. The dielectric constant for each layer is presented as a derived parameter, using the standard Langevin equations for plasma media.

The plasma layer data in Table A1 was used in calculating the self admittance (normalized relative to the waveguide admittance) of the slot antennas from both the Avco and the CAL computer programs, given in Table A2. The isolation, defined as the ratio of the received power at the matched detector in the coaxial input of one waveguide-fed slot antenna to the transmitted (radiated) power from the other, is derived from the CAL computer program. (This isolation factor neglects reflection losses in the transmitting antenna.) The load admittance for the receiving antenna is the complex conjugate of its terminal admittance under freespace transmitting conditions, as explained in Sec. 5.1. An additional parameter, the electromagnetic boundary layer thickness δ , is obtained from the plasma layer data of Table A1 as the distance from the ground plane to the point where the electron density reaches the critical value at the operating frequency.

Table A2. Admittance and Isolation of Slot Antennas Versus Altitude

Altitude (kft)	Self Admittance		Isolation (dB)	Boundary Layer δ (mm)
	CAL Program	Avco Program		
Freespace	0.191 + i0.080	0.201 + i0.035	-31.1	-
200	1.022 - i4.13	2.980 - i4.45	-37.4	0.45
220	0.544 - i1.36	0.750 - i1.55	-49.4	0.60
240	0.168 - i1.04	0.257 - i1.42	-44.9	1.00
250	0.185 - i0.89	0.593 - i1.18	-38.9	1.50
260	0.157 - i0.32	0.264 - i0.45	-21.8	2.00
275	0.163 - i0.05	0.164 - i0.10	-32.1	3.70

A parametric study was made, as mentioned in Sec. 6, to determine the effects of variations in the electron density profile between the critically dense plasma layer and the surface of the nose cone. Six different electron density profiles, having the electrical properties listed in Table A3, were selected for comparison with the 'standard profile' of Table A1 for an altitude of 240 kft. The top six layers, including the overdense sixth layer, were kept constant but the electron density in the lower two or three layers were varied from an insignificant value to about one half the critical value.

Table A3. Parametric Variation in Electrical Properties of Plasma Layers at Stagnation Point (altitude = 240 kft)

Model	Slab No. *	Slab Width (cm)	Electron Density $e1/m^3$	Collision Frequency (sec^{-1})	Dielectric Constant	
					Real	Imag.
Standard Profile	1	0.075	0.15E 16	0.10E 11	0.988	0.006
	2	0.050	0.56E 16	0.10E 11	0.957	0.024
	3	0.075	0.20E 17	0.10E 11	0.847	0.085
	4	0.100	0.30E 18	0.10E 11	-1.291	1.288
	5	0.300	0.22E 19	0.15E 10	-20.750	1.852
	6	0.075	0.20E 19	0.15E 10	-0.996	0.168
	7	0.050	0.10E 16	0.50E 09	0.989	0.000
	8	0.025	0.	0.	0.999	0.
A	7	0.030	0.50E 17	0.50E 09	0.497	0.014
	8	0.040	0.30E 17	0.50E 09	0.698	0.008
	9	0.005	0.	0.	0.999	0.
B	7	0.030	0.30E 17	0.50E 09	0.698	0.008
	8	0.040	0.10E 17	0.50E 09	0.899	0.002
	9	0.005	0.	0.	0.999	0.
C	7	0.070	0.50E 17	0.50E 09	0.497	0.014
	8	0.005	0.	0.	0.999	0.
D	7	0.070	0.10E 16	0.50E 09	0.989	0.000
	8	0.005	0.	0.	0.999	0.
E	7	0.070	0.30E 17	0.50E 09	0.698	0.008
	8	0.005	0.	0.	0.999	0.
F	7	0.070	0.10E 17	0.50E 09	0.899	0.002
	8	0.005	0.	0.	0.999	0.

*The first 6 slabs for all models are the same as those for the standard profile.

The results of the self admittance calculations for these model profiles listed in Table A4, indicate that the power reflection coefficient in the waveguide varies by less than 10 percent for this wide range of electron densities in the underdense region of the plasma sheath.

Table A4. Parametric Variation in Admittance and Reflection Coefficient of Slot Antennas (alt = 240 kft)

Model	Self Admittance Normalized (CAL Program)	Power Reflection Coefficient, R_p	VSWR
Standard Profile	0.168 - i1.04	0.725	12.4
A	0.199 - i1.10	0.699	11.2
B	0.177 - i1.06	0.717	12.0
C	0.224 - i1.14	0.679	10.3
D	0.168 - i1.04	0.725	12.4
E	0.185 - i1.07	0.711	11.7
F	0.171 - i1.05	0.722	12.3

Appendix B

Polarization Factor for Radiation Pattern of Nose Cone Antenna

The intensity of the signal received at the ground station from the antenna at the stagnation point of the nose varies with aspect angle in accordance with two factors: (a) the amplitude $g(\theta, \phi)$, which depends only on the radiation pattern of the nose cone antenna, (b) the polarization $p(\theta, \phi)$, which depends on the degree of cross polarization between the nose cone antenna and the ground antenna. This appendix derives the expression for the polarization factor, $p(\theta, \phi)$.

Both the transmitting antenna on the nose cone and the paraboloidal reflector antenna at the ground receiver site are assumed to be linearly polarized. The received electric field E_p is thus proportional to the scalar product of a unit vector \vec{e} in the plane of polarization of the nose cone antenna and a unit vector \vec{p} in the plane of polarization of the ground reflector antenna:

$$E_p \propto \vec{e} \cdot \vec{p} . \quad (B1)$$

The polarization factor

$$p(\theta, \phi) = \vec{e} \cdot \vec{p} . \quad (B2)$$

The geometric relations between unit vectors are shown in Figure B1. Here the nose cone antenna, located at the origin, is fixed with respect to a coordinate system that has rectangular components x, y, z , with the slot aperture lying in the

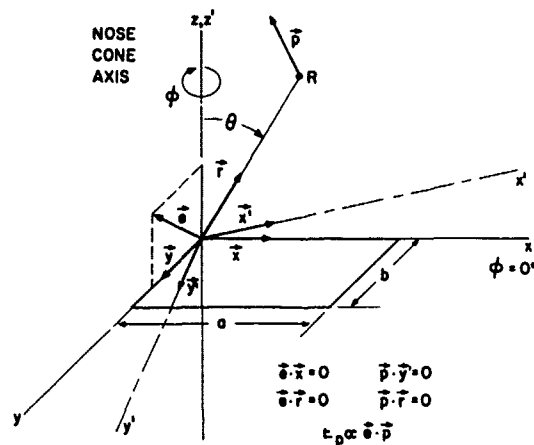


Figure B1. Polarization Diagram for Radiation Patterns

x-y plane. The z axis of this coordinate system is coincident with the longitudinal axis of the nose cone, and so rotation of the nose cone results in spatial rotation of its x and y, but not its z, components. The ground receiver antenna, located at point R, is fixed with respect to a coordinate system that has primed rectangular components x' , y' , z' , where z' is taken as the local vertical on the earth's surface. The nose cone is assumed to reenter in a vertical trajectory, and so the z and z' axis of the two coordinate systems coincide. (The nose cone actually reenters with its longitudinal axis inclined between 10° and 20° to the vertical. This difference produces only a slight change in the polarization factor, which could have been taken into account in the analysis by assuming an angle of inclination between the z and z' axis.) Rotation of the nose cone by an angle ϕ therefore corresponds to rotation of the x and y coordinates by the same angle, relative to the x' - y' coordinates.

Several relations can now be expressed between the polarization vectors \vec{e} and \vec{p} and the unit coordinate vectors. Since the polarization vector \vec{e} of the nose cone antenna lies in the y-z plane,

$$\vec{e} \cdot \vec{x} = 0. \quad (\text{B3})$$

The polarization vector \vec{e} must also be perpendicular to the radius vector \vec{r} between the nose cone antenna and the ground receiving site, so

$$\vec{e} \cdot \vec{r} = 0. \quad (\text{B4})$$

Likewise, the polarization vector \vec{p} for the ground antenna lies in the $x'-z'$ plane. Thus,

$$\vec{p} \cdot \vec{y}' = 0, \quad (\text{B5})$$

and is perpendicular to the radius vector \vec{r} , so

$$\vec{p} \cdot \vec{r} = 0. \quad (\text{B6})$$

Equations (B2) through (B6) are now solved simultaneously to obtain the polarization factor $g(\theta, \phi)$. The following relations can be written between the unit coordinate vectors ($\vec{x}, \vec{y}, \vec{z}$ and $\vec{x}', \vec{y}', \vec{z}'$), the coordinate angles θ and ϕ , and the radius vector \vec{r} :

$$\begin{aligned} \vec{x}' &= \vec{x} \cos \phi + \vec{y} \sin \phi, \\ \vec{y}' &= -\vec{x} \sin \phi + \vec{y} \cos \phi, \\ \vec{z}' &= \vec{z}, \\ \vec{r} &= \vec{x}' \sin \theta + \vec{z}' \cos \theta \\ &= (\sin \theta \cos \phi) \vec{x} + (\sin \theta \sin \phi) \vec{y} + (\cos \theta) \vec{z}. \end{aligned} \quad (\text{B7})$$

The polarization vectors \vec{e} and \vec{p} , expressed as linear combinations of the unit vectors for the x, y, z coordinate system, are:

$$\begin{aligned} \vec{e} &= a\vec{x} + b\vec{y} + c\vec{z}, \\ \vec{p} &= d\vec{x} + e\vec{y} + f\vec{z}, \end{aligned} \quad (\text{B8})$$

where the coefficients are yet to be determined.

From Eqs. (B3) and (B8),

$$\vec{e} = b\vec{y} + c\vec{z}, \quad (a = 0). \quad (\text{B9})$$

Since \vec{e} is a unit vector,

$$b^2 + c^2 = 1. \quad (\text{B10})$$

From Eqs. (B4), (B7), and (B9),

$$b \sin \theta \sin \phi + c \cos \theta = 0. \quad (\text{B11})$$

B4

From Eqs. (B5), (B7), and (B8),

$$-d \sin \phi + e \cos \phi = 0 . \quad (\text{B12})$$

From Eqs. (B6), (B7), and (B8),

$$d \sin \theta \cos \phi + e \sin \theta \sin \phi + f \cos \theta = 0 . \quad (\text{B13})$$

Since \vec{p} is a unit vector,

$$d^2 + e^2 + f^2 = 1 . \quad (\text{B14})$$

From Eqs. (B12) and (B13),

$$e \frac{\sin \theta}{\sin \phi} + f \cos \theta = 0 . \quad (\text{B15})$$

From Eqs. (B10) and (B11),

$$c = \frac{\sin \theta \sin \phi}{\left[1 - \sin^2 \theta (1 - \sin^2 \phi) \right]^{1/2}} ; \quad (\text{B16})$$

$$b = \frac{-\cos \theta}{\left[1 - \sin^2 \theta (1 - \sin^2 \phi) \right]^{1/2}} . \quad (\text{B17})$$

From Eqs. (B12), (B14), and (B15),

$$e = \cos \theta \sin \phi ; \quad (\text{B18})$$

$$f = -\sin \theta . \quad (\text{B19})$$

Combining Eqs. (B2), (B16), (B17), (B18), and (B19) yields the polarization factor:

$$\begin{aligned} p(\theta, \phi) &= \left| \vec{e} \cdot \vec{p} \right| = \left| (be + cf) \right| \\ &= \frac{\sin \phi}{\left[1 - \sin^2 \theta (1 - \sin^2 \phi) \right]^{1/2}} , \end{aligned}$$

which is Eq. (18) of Sec. 5.

UNCLASSIFIED
Security Classification

DOCUMENT CONTROL DATA - R&D		
(Security classification of title, body of abstract and indexing annotation must be entered when the overall report is classified)		
1. ORIGINATING ACTIVITY (Corporate author) Air Force Cambridge Research Laboratories (CRD) L.G. Hanscom Field Bedford, Massachusetts 01730		2a. REPORT SECURITY CLASSIFICATION Unclassified
		2b. GROUP
3. REPORT TITLE EFFECTS OF THE REENTRY PLASMA SHEATH ON MICROWAVE ANTENNA PERFORMANCE: TRAILBLAZER II ROCKET RESULTS OF 18 JUNE 1967		
4. DESCRIPTIVE NOTES (Type of report and inclusive dates) Scientific. Interim.		
5. AUTHOR(S) (First name, middle initial, last name) Leon J. Poirier, Walter Rotman, Dallas T. Hayes, and John F. Lennon		
6. REPORT DATE August 1969	7a. TOTAL NO. OF PAGES 74	7b. NO. OF REFS 33
8a. CONTRACT OR GRANT NO.		9a. ORIGINATOR'S REPORT NUMBER(S)
b. PROJECT, TASK, WORK UNIT NOS. 4642-01-01		AFCRL-69-0354
c. DOD ELEMENT 62101F		9b. OTHER REPORT NO(S) (Any other numbers that may be assigned this report)
d. DOD SUBELEMENT 681000		PSRP No. 394
10. DISTRIBUTION STATEMENT 2-This document is subject to special export control, and each transmittal to foreign governments or persons abroad may be made only with prior approval of AFCL, CRD, L.G. Hanscom Field, Bedford, Massachusetts.		
11. SUPPLEMENTARY NOTES TECH, OTHER		12. SPONSORING MILITARY ACTIVITY Air Force Cambridge Research Laboratories (CRD) L.G. Hanscom Field Bedford, Massachusetts 01730
13. ABSTRACT An AFCRL Trailblazer II rocket was launched on 18 June 1967 from the NASA Wallops Island (Va.) Rocket Test Facility to study the properties of the reentry plasma sheath and its effects on microwave antenna performance. The reentry payload consisted of three major subsystems: a plasma diagnostic system, an S-band transponder system, and an X-band telemetry system. The flight data yielded (1) measurements of the influence of the plasma on the radiation pattern distortion, signal attenuation, and impedance mismatch for an S-band slot antenna located at the stagnation point of the nose cone; (2) measurements of the plasma sheath effects on the interantenna coupling between two S-band antennas on the nose cone; and (3) determinations of the electron density profile and gradients in the boundary layer about the nose cone. These measurements indicated that electron density profiles in the flow fields can be determined from electrostatic and electroacoustic probe data. The microwave antenna data was in substantial agreement with the probe data and flow field calculations, with the best agreement obtained at altitudes below 240 kft. The shape of the radiation patterns of the S-band antennas remained invariant with altitude, in accord with the theory of microwave interaction with a thin plasma layer.		

DD FORM 1 NOV 68 1473

UNCLASSIFIED
Security Classification

UNCLASSIFIED

Security Classification

14.	KEY WORDS	LINK A		LINK B		LINK C	
		ROLE	WT	ROLE	WT	ROLE	WT
	Reentry Communications Trailblazer Vehicle Plasma Sheath Microwave Antennas Reentry Vehicles Plasma Diagnostics						

UNCLASSIFIED

Security Classification